Parkinson's disease LRRK2 mutations dysregulate iron homeostasis and promote oxidative stress and ferroptosis in human neurons and astrocytes

Adamantios Mamais[1]*, Richard D. Batchelor Jr[1], Aravindraja Chairmandurai[1], Thomas B. Ladd[1], Austin J. Shute[1], Nitya Subrahmanian[1], Nunziata Maio[2], Christopher D. Vulpe[3], Matthew J. LaVoie[1]*.

1. Center for Translational Research in Neurodegenerative Disease, Fixel Institute for Neurologic Diseases, Department of Neurology, University of Florida, Gainesville, FL, USA.
2. *Eunice Kennedy Shriver* National Institute of Child Health and Human Development, NIH, Bethesda, MD, USA.
3. Center for Environmental and Human Toxicology, Department of Physiological Sciences, College of Veterinary Medicine, University of Florida, Gainesville, FL, USA.

* To whom correspondence should be addressed: Adamantios Mamais (a.mamais@ufl.edu) and Matthew J. LaVoie (mlavoie@ufl.edu)

Abstract

Background: Iron accumulation is a hallmark of sporadic and familial Parkinson's disease (PD) and correlates with clinical motor symptom severity. The biochemical mechanisms driving iron dyshomeostasis in PD brain and whether these are early or late events in the neurodegenerative process remain unknown. Nigral iron levels in LRRK2-PD patients have been reported to be even higher than in idiopathic PD, and greater in non-manifesting LRRK2 carriers than controls, suggesting that iron accumulation precedes clinical onset in LRRK2-associated PD. However, the cells affected and mechanisms governing iron dyshomeostasis in PD remain unclear.

Methods: Here, we investigated multiple independent measures of iron homeostasis in iPSCs, iPSC-derived cortical and dopaminergic neurons, and astrocytes from control and PD patient-derived iPSCs and an isogenic iPSC panel of three independent pathogenic PD mutations. High-content and super-resolution microscopy of iron-specific probes and ICP-MS were used to determine iron content and distribution across different cell types and LRRK2 genotypes. The upstream effectors and downstream consequences of iron dyshomeostasis on ferroptosis signaling were also examined.

Results: We found that heterozygous LRRK2 mutations dysregulate cellular iron levels across iPSCs, neurons and astrocytes, in a kinase-dependent manner. Lysosomal ferrous iron was specifically and consistently elevated across iPSCs, iPSC-derived cortical and dopaminergic neurons, and astrocytes carrying LRRK2 mutations and rescued by treatment with the selective LRRK2 inhibitor, MLi-2. Importantly, we show that lipid peroxidation and ROS levels are elevated in isogenic LRRK2 mutant neurons, while iron chelation or MLi-2 reduced LRRK2-dependent ROS damage. LRRK2 regulates the function of over a dozen Rab GTPase proteins through direct phosphorylation, and our prior work revealed a unique correlation with Rab8a trafficking and iron. Here, we report that CRISPR/Cas9 knockout of Rab8a recapitulates LRRK2-driven effects on intracellular iron in different cell types and that exogenous Rab8a normalizes lysosomal iron levels in R1441C LRRK2 iPSCs.

Conclusions: Together, our findings demonstrate that LRRK2 mutations disrupt iron homeostasis across multiple cell types, including dopaminergic neurons, and establish a discrete biochemical pathway linking LRRK2 and vulnerability to ferroptosis signaling.

Keywords

LRRK2, Parkinson's disease, iron, lysosomes, ferroptosis, Rab8a, iPSC, neurons, astrocytes

Background

Iron accumulation in the substantia nigra is a well-recognized pathological hallmark of Parkinson's disease (PD), observed in both sporadic and familial forms of the disorder and in other neurodegenerative conditions (1–7). Iron overload correlates with neuromelanin loss in post-mortem PD brains (8) and is detectable *in vivo* through advanced MRI techniques, such as quantitative susceptibility mapping (QSM), where iron deposition in the substantia nigra pars compacta (SNc) has been correlated with motor symptom severity (9). Notably, iron-sensitive imaging aids in distinguishing PD from other parkinsonian syndromes such as multiple system atrophy (MSA) and progressive supranuclear palsy (PSP) (10–14). Despite decades of evidence linking iron dyshomeostasis to PD, the molecular underpinnings that drive brain iron accumulation and neuronal vulnerability and whether these are early or late features of disease remain incompletely understood.

Iron's potential to promote oxidative stress through Fenton chemistry and the generation of reactive oxygen species (ROS) make it a likely contributor to dopaminergic (DA) neuron degeneration (15,16). Ferroptosis, a regulated form of iron-dependent cell death, has emerged as a key mechanism linking iron overload to neuronal loss (17–19) and has been widely implicated in PD (20–24), but how genetic factors for PD intersect with ferroptotic pathways is not fully defined. Mutations in leucine-rich repeat kinase 2 (LRRK2) are the most common cause of familial PD (25) and have been implicated in vesicular trafficking defects and lysosomal dysfunction (26–32), processes that could plausibly disrupt iron handling. Indeed, clinical imaging studies reveal that individuals carrying pathogenic LRRK2 mutations, whether symptomatic or asymptomatic, exhibit elevated nigral iron levels compared to idiopathic PD patients and healthy controls (33), suggesting that iron dyshomeostasis could be an early and contributing feature in LRRK2-associated PD. However, the cellular and molecular mechanisms underlying these clinical observations remain unknown.

Autosomal dominant missense mutations in LRRK2 cause a late-onset form of familial PD while genome-wide association studies have identified risk-factor variants of LRRK2 linked to idiopathic PD (25). PD-linked mutations segregate within the kinase domain (e.g. G2019S) and the Roc-COR tandem domain (e.g. R1441C, Y1699C) of LRRK2 and increase phosphorylation of over a dozen Rab GTPase substrates at a conserved threonine/serine residue (34,35) disrupting intracellular trafficking and endolysosomal dynamics (26–29). Given that Rab GTPases govern critical steps in membrane trafficking and receptor recycling (36), these

pathways offer a potential intersection between LRRK2 function and iron regulation. In our previous work, we observed alterations in trafficking of the transferrin receptor (TfR), that mediates iron uptake in most cell types (37–40), in mutant LRRK2 overexpression models (32). Importantly, we reported an increase in brain ferritin and iron load in homozygous G2019S KI mice compared to WT controls in acute pro-inflammatory conditions (32). Whether such disturbances occur basally and across different LRRK2 mutations, particularly in human neurons and glia when expressed in the heterozygous state, remains unclear. Astrocytes are key regulators of brain iron levels and availability and are implicated in PD neuropathology (41–47). Furthermore, LRRK2 expression is enriched in astrocytes and we and others have reported effects of LRRK2 mutations on astrocytic function (48,49). How endogenous LRRK2 mutations specifically affect cellular iron status and distribution in human astrocytes and neurons as well as the role of altered iron in neuronal damage remain unexplored.

In this study, we leverage patient-derived and isogenic induced pluripotent stem cell (iPSC) models to investigate how pathogenic LRRK2 mutations influence iron regulation in human neurons and astrocytes. By examining a wide panel of iron-related phenotypes, our data revealed convergent effects of heterozygous R1441C, Y1699C and G2019S LRRK2 mutations on intracellular and lysosomal iron content that were rescued by LRRK2 inhibition. Furthermore, we report distinct effects of LRRK2 mutations on ferritin levels and a concomitant effect on basal Iron Regulatory Protein Iron-Responsive-Element (IRE)-binding activity, suggesting alterations in ferritin expression and or post-transcriptional regulation. Pathogenic LRRK2 kinase activity is thought to inactivate Rab8a, which showed a special relationship with cellular iron. Genetic Rab8a deficiency recapitulated key iron-related defects observed in LRRK2 mutant cells, while exogenous Rab8a expression normalized lysosomal iron levels in heterozygous R1441C LRRK2 cells. Basal ROS levels and lipid peroxidation were elevated in LRRK2 mutant neurons and reduced by iron chelation or LRRK2 kinase inhibition. Importantly, kinase-dependent increases in lysosomal iron and lipid peroxidation were observed in LRRK2-mutant dopamine (DA) neurons, supporting the engagement of ferroptotic signaling in this cellular model of PD. Our data highlight a discrete pathway affected by pathogenic LRRK2 mutations that results in the misregulation of this transitional metal, leading to cellular injury. These data suggest a central role for iron dyshomeostasis in the interplay between LRRK2 signaling and ROS reported across many PD models and thought to contribute to PD (50–52), .

Methods

Induced pluripotent stem cell (iPSCs) cultures

We used iPSC lines carrying heterozygous LRRK2 mutations from three independent sources. BR33 were derived from a Caucasian donor, who was deeply phenotyped as part of the ROS/MAP longitudinal aging studies (53,54) and determined to not be cognitively impaired at death at age >89 and free from genetic variants that confer risk of PD. ND35371 (R1441C heterozygous) and ND50051 (G2019S heterozygous) were obtained by the NINDS Repository. Five G2019S heterozygous, two R1441G heterozygous and five WT iPSC lines were obtained from the Parkinson's Progression Markers Initiative dataset (PPMI, ppmi-info.org) along with longitudinal clinical data. The isogenic mutant LRRK2 lines (all heterozygous) were a kind gift from Dr. Mark Cookson (NIA, NIH) (55).

CRISPR/Cas9 Genome Editing of iPSCs and HEK293 cells

Rab8a and Rab10 knockout lines were generated in iPSCs and HEK293 cells as described before (56). Briefly, single guide RNAs (sgRNAs) were selected using a web-based design tool (http://crispr.mit.edu). Rab8a sgRNA: 5' GAACTGGATTCGCAACATTG 3'; Rab10 sgRNA: 5' ATGGCTTAGAAACATAGATG 3'. These were cloned into pXPR_003 (Addgene #52963) and sequenced using the primer 5′-GATACAAGGCTGTTAGAGAGATAATT-3′ to determine clones that successfully integrated the sgRNA. BR33 iPSCs were generated and characterized in collaboration with the New York Stem Cell Foundation (NYSCF) using described methods (54,57,58). iPSCs were co-transfected with plasmids that express the sgRNA plasmid and a nuclease-active SpCas9 expression vector (Addgene #62988). After 2 days, cells that were successfully transfected with the two plasmids were selected by puromycin treatment for 4 days. Individual clones were identified by plating ~1 cell per well in a 96-well dish and allowed to grow for 2 weeks. Monoclonal lines were identified, expanded, sequenced, and stocked. Amplification of Rab8a and Rab10 genes was conducted according to manufacturer's protocol (Invitrogen K2030-01) and homozygous gene editing was confirmed by Sanger sequencing. Multiple sequence alignment was performed using ClustalW in BioEdit.

iPSC differentiation into mature astrocytes

iPSCs were differentiated into iAs using the protocol developed by Canals and colleagues (59). Briefly, iPSCs were maintained in mTeSR media and transduced with lentivirus to stably express pTet-O-NFIB (hygromycin), pTet-O-SOX9 (puromycin) and FUdelta GW-rtTA. Differentiation of pure human iA cultures was achieved by culturing transduced cells in

doxycycline to induce expression of Sox9 and Nfib and to select against non-differentiated cells with selection media (puromycin and hygromycin). Human iAs were studied at day ~21 post-differentiation. iAs show marked expression of GFAP by staining and immunoblot and robust expression of LRRK2 and relevant Rab GTPases.

Differentiation of NGN2-induced neurons

iPSCs were differentiated into NGN2-induced neurons (iNs), as before (29,56,60). Briefly, iPSCs were cultured on Matrigel-coated plates in StemFlex (A33493) media and co-transduced with lentivirus packaged with pTet-O-NGN2-puro and Fudelta GW-rtTA plasmids (Zhang et al., 2013) for 2 days and passaged for expansion. NGN2-transduced iPSCs were thawed in StemFlex media with ROCK inhibitor (10 μM; Stemcell Technologies, 72304) for 24 hr then plated at 2×10^6 cells/10 cm plate in StemFlex and grown until 75% confluent. For differentiation, on day 1 cells were fed with KnockOut media (Gibco 10829.018) supplemented with KnockOut Serum Replacement (Invitrogen 10928-028), 1% MEM non-essential amino acids (Invitrogen 11140), 1% GlutaMAX (Gibco 35050061) and 0.1% βME (Invitrogen 21985-023) (KSR) with doxycycline (2 μg/ml, Sigma, D9891-5g) to induce NGN2 expression. On day 2, they were fed with a 1:1 ratio of KSR:N2B media (DMEM F12 supplemented with 1% GlutaMAX, 3% dextrose and N2-Supplement B; StemCell Technologies 07156) with puromycin (5 μg/ml; Life Technologies, A11138-03) and doxycycline to select for transduced cells. On day 3, the cells were fed with N2B media with B27 (1:100; Life Technologies, 17504-044), puromycin, and doxycycline. On day 4, induced neurons (iNs) were frozen down in 10% DMSO/FBS in Neurobasal media (NBM Gibco 21103-049) supplemented with B27, BDNF (Peprotech, 450-02), CNTF (Peprotech, 450-13), and GDNF (Peprotech, 450-10) all at 100 ng/uL, ROCK inhibitor (10 μM), puromycin, and doxycycline. iNs were plated and grown in NBM with B27, BDNF, CNTF, GDNF, puromycin, and doxycycline until day 21.

iPSC differentiation into DA neurons

iPSCs were cultured in StemFlex (A33493) media and co-transduced with lentivirus packaged with pTet-O-NGN2-puro and Fudelta GW-rtTA plasmids for 2 days and passaged for expansion, as before(29,56,60). To begin the dopaminergic neuron destination, NGN2-transduced iPSCs were thawed in mTeSR Plus media (StemCell technologies,100-0276) with 10 μM ROCK inhibitor (StemCell Technologies, 72304) and plated at 2×10^6 cells/10 cm plate coated with Matrigel (Corning, 354277) and grown to 75% confluency - considered Day -1 (D-1). The iPSCs were differentiated into mature dopaminergic neurons using established protocols(61,62). Briefly, at D0 the cells were treated media containing growth factors and 2 μg/mL Doxycycline

(ThermoFisher, J6057914) (Dox; present through differentiation) to begin the differentiation and Puromycin (ThermoFisher, A1113803) was added to the formulation for D1. On D2, cells were plated in media with containing growth factors and Dox with ROCK inhibitor at 5 x 10^4 cells/well in 96 well plates (Griener, 655090) coated with Poly-L-ornithine hydrobromide (Sigma-Aldrich, P3655) - Laminin (Sigma-Aldrich, CC095-M). STEMdiff Midbrain Neuron Differentiation (Kit) media (StemCell Technologies, 100-0038) was used on D3 & D4 supplemented with Dox, 1 µM Cytarabine (Sigma-Aldrich, 251010), and 200 ng/mL SHH (StemCell Technologies, 78065). Daily media changes continue D5-D8 in the presence of Dox and SHH. D9-D21, cells were cultured using STEMdiff Midbrain Neuron Maturation (Kit) media (StemCell Technologies, 100-0038) with half media changes every third day.

PPMI UPDRSIII data

Data used in the preparation of this article was obtained from the Parkinson's Progression Markers Initiative (PPMI) database (www.ppmi-info.org/access-data-specimens/download-data), RRID:SCR_006431. Openly available UPDRSIII data for five G2019S and two R1441G mutations carriers were used (Tier 1 data downloaded between 03 November 2023 and 10 November 2023).

IRE-binding activity assays

IRP activity was assessed using biotinylated IRE RNA probes, as previously described (63). Briefly, probes were 3'-biotinylated and sourced from Eurofins Genomics or IDT. Cell or tissue lysates were prepared in lysis buffer (40 mM KCl, 25 mM Tris-Cl pH 7.5, 1% Triton X-100) with protease inhibitors (ThermoFisher #78430), 1 mM DTT, and 20 U/ml RNase inhibitor (ThermoFisher #AM2696). For binding, 5 pmol of annealed IRE probes were incubated with 100 µg DynaBeads M280 for 20 min at room temperature, washed three times, then mixed with 100 µg lysates for another 20 min. IRP-bound complexes were isolated magnetically, washed, and resuspended in 100 µL LDS buffer, denatured at 95 °C for 5 min, and analyzed by western blot (25 µL on 4-12% Bis-Tris gels) for IRP1 and IRP2.

ICP-MS

iPSCs in culture were collected in ice-cold PBS and divided equally into two tubes for ICP-MS and biochemical analysis of protein levels, pelleted and frozen in dry ice. Frozen iPSC pellets were resuspended in 200 µl PBS and mixed with 200 µl of concentrated trace-metal-grade nitric acid (Fisher) in 15 ml Falcon tube. The samples were digested at 85°C overnight, diluted to 4 ml with deionized water, and then analyzed by Agilent 7900 ICP-MS at the Analytical Toxicology

Core Laboratory (ATCL) at the University of Florida. Metal levels were normalized to total protein content.

Cell Treatments

For iron overload or chelation, cells were treated with 150 μM ferric ammonium citrate (FAC) (SIGMA) or 100 μM of deferoxamine in normal media overnight prior to analysis by imaging or western blotting. For rescue experiments, cells were treated with 100 nM MLi-2 (Tocris) for 2 hrs or 7 days in culture prior to analysis.

iPSC transfection

Human iPSCs were transiently transfected with GeneJuice (Millipore) at ~60-70% confluency using a 3:1 μL GeneJuice:μg DNA ratio prepared in Opti-MEM (ThermoFisher). DNA-GeneJuice complexes were added directly to cells in mTeSR1 medium, and transgene expression and cellular analyses were performed 24-48 hours post-transfection. The constructs eGFP-Rab8a (Addgene #86075) (64) and pcDNA3.1 eGFP (Addgene #129020) were used.

Western Blot

Cells were lysed in cell lysis buffer (50 mM Tris-HCl, 150 mM NaCl, 0.5 mM EDTA, 0.5% (v/v) sodium deoxycholate, 1% (v/v) NP-40, pH 8) with protease and phosphatase inhibitors for 30 min. Lysates were centrifuged at 14,000 x *g* for 15 min at 4°C, and supernatants were quantified by BCA assay. Samples were prepared in 1x SDS-PAGE loading buffer, denatured at 65°C for 10 min, resolved on an SDS-polyacrylamide gel, and transferred to PVDF membrane. Membranes were blocked with 5% BSA (Sigma) prior to probing with primary antibodies against FTH1 (Cell Signaling 4393S), FTL (abcam AB69090), TfR1 (13-6800), DMT1 (abcam AB123085), Cyclophilin B (abcam AB16045). Secondary LiCOR antibodies were used for detection using the LiCOR model M scanner. Uncropped blots are presented in Supplementary Figure 10.

Immunocytochemistry

Cells were seeded at 120,000/well (24-well plate) on 12 mm coverslips precoated with Geltrex basement membrane matrix (A1413201, Thermo) and cultured as described above. Cells were fixed in 4% (w/v) formaldehyde/PBS for 15 minutes, permeabilized in 0.2% Triton X-100/PBS for 10 minutes at RT, blocked in 5% (v/v) FBS in PBS, and incubated with primary antibodies (pT73 RAB10: MJF-R21-22–5, ab241060, Abcam; TH: CPC-TA, EnCor Bio) in 1% (v/v) FBS/PBS overnight at 4C. Following 3 washes in PBS, the cells were incubated for 1 hour with secondary

antibodies (Alexa Fluor 488, 568, 647-conjugated; ThermoFisher). After 3 PBS washes, the coverslips were mounted, and the cells were imaged by confocal microscopy (Nikon CSU-W1-SORA).

High-content imaging and quantitative analysis

For high-content live-cell imaging, cells were plated at 10,000 cells per well in 96-well black-wall clear-bottom plates (µClear, Greiner), labeled with FerroOrange (Dojindo), HMRhoNox-M (Lumiprobe), Liperfluo (Thermo), LysoTracker Red (Invitrogen) and CellROX (Thermo) according to the manufacturer's specifications, and 20 ng/ml of Hoechst. CellLight Lamp1-emGFP BacMam 2.0 or LysoTracker (Thermo) were used to visualize lysosomes according to the manufacturer's specifications. Labeled live cells were imaged using the Lionheart high-content automated microscope (Agilent) (10x or 20x objectives), or the ImageXpress HCS.ai high-content confocal imaging platform (Molecular Devices; 60x objective), collecting multiple fields per well for coverage of >800 cells per well. The DAPI, GFP, RFP/TRITC and Cy5 channels were used and images were analyzed on the Gen5 software (Lionheart; Agilent) or InCarta software (Molecular Devices). For experiments involving GFP control vector or GFP-Rab8a expression, quantitative analyses were restricted to GFP-positive cells to ensure consideration of successfully-transfected cells. To account for plate-to-plate variability in staining intensity, fluorescence measurements were normalized to the corresponding control condition within each imaging plate before pooling data across biological replicates.

Quantification of lysosomal iron using whole-cell, lysosome-restricted segmentation

Quantitative analysis of HMRhoNox-M fluorescence was performed using the InCarta image analysis software (Molecular Devices) using two complementary segmentation strategies. For whole-cell analysis, nuclei were identified using Hoechst staining and used as primary objects. Cytoplasmic regions were generated based on the primary objects (nuclei) using TRITC staining for cell perimeter, producing a whole-cell mask for quantification of integrated HMRhoNox-M signal on a per-cell basis. For lysosome-restricted analysis, lysosomes were identified using LysoTracker staining. LysoTracker-positive puncta were segmented as subcellular objects using intensity-based thresholding and size filtering, producing a lysosomal mask per cell (similar to(65)), and HMRhoNox-M signal was quantified within lysosomes. Measurements were aggregated across multiple fields per well, with >800 cells analyzed per biological replicate.

Imaris analysis

Following confocal microscopy, the Imaris platform (Oxford Instruments) was used to analyze the localization and distribution of lysosomal iron in lysosomes. Z-stack confocal images of iAs were processed through the Imaris Surface Contour module to render lysosomal iron, lysosomes and nuclear staining to surfaces and measure the distance between lysosomes and proximity to the nuclear edge throughout z planes in the 3D volume.

Statistical Analyses

All experiments were conducted at least three independent times for three differentiations. Error bars indicate mean +SD. Statistical analysis was performed using GraphPad Prism software, using a one-way ANOVA with Dunnett's post-hoc or two-way ANOVA with Tukey's post-hoc test.

Results

LRRK2 mutations dysregulate iron-related pathways in patient-derived and isogenic iPSCs and neurons in a kinase-dependent manner

In our previous work, we identified a signature of altered iron pathways in the kidneys of homozygous G2019S knockin mice by unbiased proteomics, highlighting divergent expression of endolysosomal and mitochondrial factors involved in iron regulation *in vivo* (35). Separately, we reported increased accumulation of iron in the brains of homozygous G2019S LRRK2 mice following inflammation compared to WT controls (32). These data were the first to suggest that G2019S LRRK2 dysregulates aspects of intracellular iron homeostasis in LRRK2 models. To examine whether these pathways are affected by endogenous LRRK2 mutations beyond G2019S, and, when present in the heterozygous state most commonly associated with PD, we assessed different aspects of iron homeostasis in iPSCs derived from LRRK2-PD patients. We quantified cytosolic iron levels in six WT, six G2019S, one R1441C, and two R1441G LRRK2 iPSC lines (all heterozygous) by high-content imaging of the FerroOrange probe, a fluorescent indicator of labile iron. We observed an increase in the steady-state labile ferrous iron pool across different LRRK2 mutant lines compared to WT lines (Figure 1A, B). Each iPSC line is depicted in a different color to reflect the biological variability observed across the many patient-derived lines (Figure 1B). Increased total iron loading in the R1441C LRRK2 mutant iPSCs was further confirmed by ICP-MS (Figure 1C). Lastly, the small molecule LRRK2 kinase inhibitor MLi-2 reversed the increase in labile iron levels in heterozygous G2019S iPSC lines compared to WT, with a partial rescue in R1441C LRRK2 iPSCs (Figure 1D, E). Next, we investigated

proteins involved in iron import (TfR1, DMT1) and iron storage (ferritin light chain; FTL). We observed an overall increase in FTL levels across the R1441C/G and G2019S mutant lines compared to WT iPSC controls (Figure 1F, G), while the levels of TfR1 and DMT1 were comparable between lines (Figure 1F and Supplementary Figure 1A, B). Despite an overall effect of mutations on iron-related readouts, we noted biological variability in the levels of labile iron (Figure 1B) and ferritin (Figure 1G) across the different patient-derived iPSC lines. We observed moderate-to-strong correlation between labile iron levels (FerroOrange) and FTL levels (R^2=0.5660, F(1,13), p=0.0012) (Figure 1H), and a strong correlation between labile iron (FerroOrange) and total iron levels detected by ICP-MS (R2=0.8805. F(1,1), p=0.2247) (Figure 1I). We did not observe a correlation between ferritin levels in the iPSC lines and motor symptom severity (UPDRS III scores) in LRRK2 PD or control groups reported for the iPSC donors (Supplementary Figure 1C).

Since iron dyshomeostasis is a key feature in PD pathology and our data support altered iron levels in LRRK2 mutant iPSCs, we next examined human iPSC-derived NGN2-induced neurons (iNs) to understand how this change translates in post-mitotic cells. iPSCs (NINDS Repository) were differentiated into iNs by forced expression of NGN2 via lentiviral gene delivery, according to established protocols (29,56,60) (Supplementary Figure 2). We detected an increase in the labile iron pool across heterozygous R1441C and G2019S LRRK2 neurons compared to WT controls (Figure 1J, K). Considering the biological variability observed in these patient-derived iPSC lines (Figure 1B), we next tested this phenotype in a series of isogenic LRRK2 mutant iPSC lines. These lines have been generated by CRISPR/Cas9 in a single female iPSC background, A18945, with editing validated and clones subsequently characterized for morphology, karyotype and differentiation potential(55). NGN2-induced neurons generated from this isogenic LRRK2 series validated the phenotype with an increase in the labile iron pool across R1441C, Y1699C and G2019S heterozygous mutant iNs, compared to WT controls (Figure 1L), supporting a generalizable effect of pathogenic LRRK2 mutations on iron homeostasis.

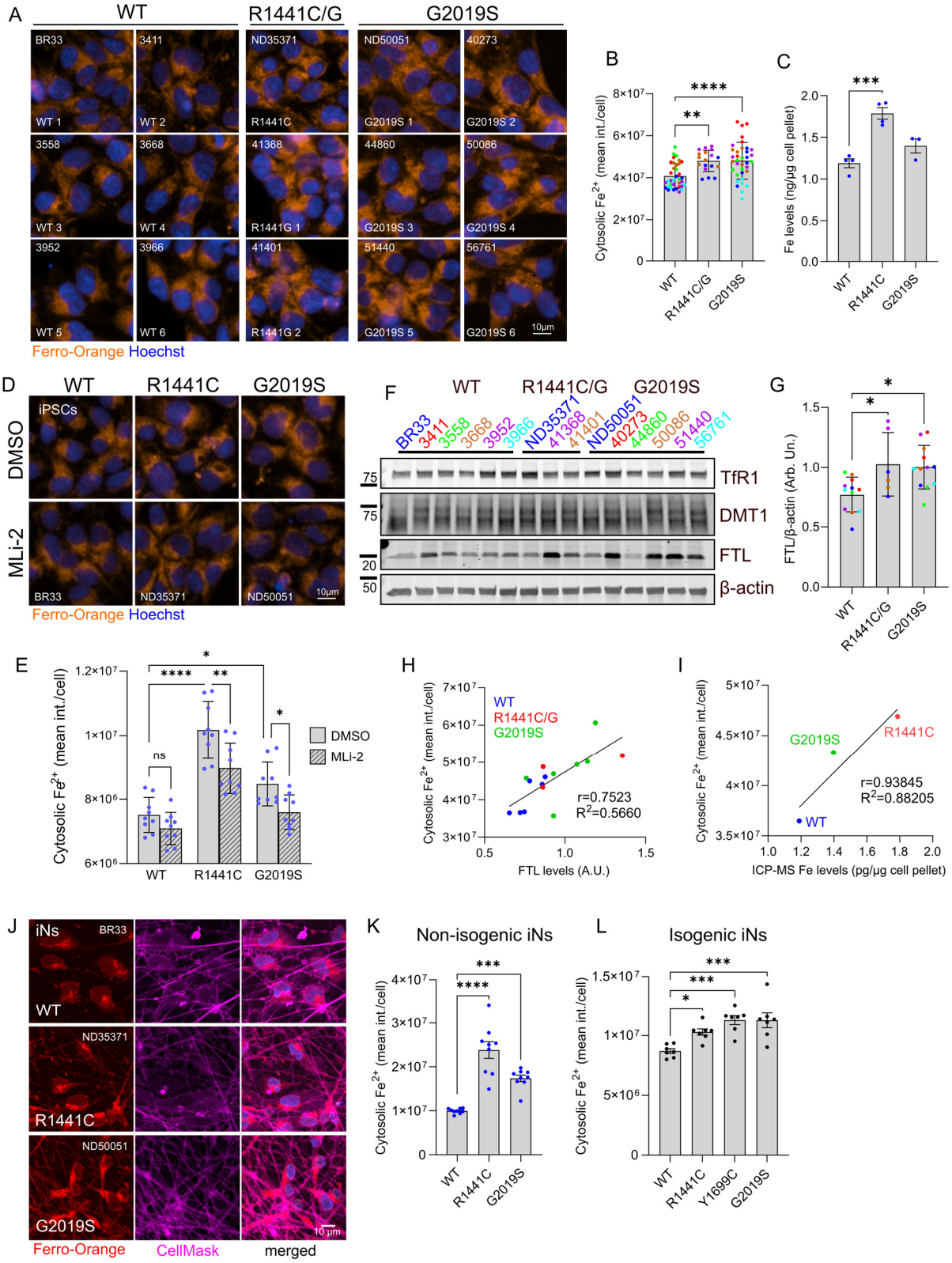
A
WT
R1441C/G
G2019S
BR33
3411
ND35371
ND50051
40273
WT 1
WT 2
R1441C
G2019S 1
G2019S 2
3558
3668
41368
44860
50086
WT 3
WT 4
R1441G 1
G2019S 3
G2019S 4
3952
3966
41401
51440
56761
WT 5
WT 6
R1441G 2
G2019S 5
G2019S 6
10μm
Ferro-Orange Hoechst
B
Cytosolic Fe2+ (mean int./cell)
8×10^7
6×10^7
4×10^7
2×10^7
0
****
**
WT
R1441C/G
G2019S
C
Fe levels (ng/μg cell pellet)
2.0
1.5
1.0
0.5
0.0
***
WT
R1441C
G2019S
D
WT
R1441C
G2019S
DMSO
MLi-2
iPSCs
BR33
ND35371
ND50051
10μm
Ferro-Orange Hoechst
F
WT
R1441C/G
G2019S
BR33
3411
3558
3668
3952
3966
ND35371
41368
41401
ND50051
40273
44860
50086
51440
56761
75
TfR1
75
DMT1
20
FTL
50
β-actin
G
FTL/β-actin (Arb. Un.)
1.5
1.0
0.5
0.0
*
*
WT
R1441C/G
G2019S
E
Cytosolic Fe2+ (mean int./cell)
1.2×10^7
1×10^7
8×10^6
6×10^6
*
****
**
*
ns
DMSO
MLi-2
WT
R1441C
G2019S
H
Cytosolic Fe2+ (mean int./cell)
7×10^7
6×10^7
5×10^7
4×10^7
3×10^7
WT
R1441C/G
G2019S
r=0.7523
R2=0.5660
0.5
1.0
1.5
FTL levels (A.U.)
I
Cytosolic Fe2+ (mean int./cell)
5×10^7
4.5×10^7
4×10^7
3.5×10^7
G2019S
R1441C
r=0.93845
R2=0.88205
WT
1.0
1.2
1.4
1.6
1.8
2.0
ICP-MS Fe levels (pg/μg cell pellet)
J
iNs
BR33
WT
ND35371
R1441C
ND50051
G2019S
10 μm
Ferro-Orange
CellMask
merged
K
Non-isogenic iNs
Cytosolic Fe2+ (mean int./cell)
4×10^7
3×10^7
2×10^7
1×10^7
0
***
****
WT
R1441C
G2019S
L
Isogenic iNs
Cytosolic Fe2+ (mean int./cell)
1.5×10^7
1×10^7
5×10^6
0
***
***
*
WT
R1441C
Y1699C
G2019S

Figure 1. LRRK2 mutations dysregulate iron-related pathways in human iPSCs and iNs in a kinase-dependent manner. (A, B) Cytosolic free iron imaging and quantitation (FerroOrange) in six WT, six G2019S, one R1441C, and two R1441G LRRK2 iPSC lines (PPMI, NINDS Repository) (N=6 wells each line; each line represented in a different color within each genotype group; one-way ANOVA, Dunnett's post-hoc pair-wise comparison). (C) Quantitation of total iron in WT, R1441C and G2019S iPSCs (NINDS Repository) by ICP-MS. (D, E) Imaging and quantitation of cytosolic free iron (FerroOrange) in mutant LRRK2 iPSCs (NINDS Repository) following Mli-2 treatment (100nM, 7 days) (two-way ANOVA, Tukey's post-hoc; N=9 biological replicates (>800 cells per N), Genotype ****p=0.0001, Treatment ****p<0.0001, Interaction p=0.2318). (F, G) Western blot and quantitation of levels of iron-related factors in WT, heterozygous R1441C/G, and G2019S iPSCs (N=2 biological replicates per line; 6 WT, 2 R1441G, 1 R1441C and 6 G2019S lines, one-way ANOVA, Dunnett's post-hoc; *p<0.05). (H) Scatter plot showing a positive correlation between cytosolic iron (FerroOrange) and FTL levels (r=0.7523). (I) Scatter plot showing a positive correlation between cytosolic ferrous iron levels (FerroOrange) and total cellular iron quantified by ICP-MS across iPSC lines. Each data point represents the mean value for a single iPSC line (WT: BR33, R1441C: ND35371, G2019S: ND50051), calculated from >4 independent biological replicates for ICP-MS and 6 independent imaging wells for FerroOrange (>800 cells per well). Pearson correlation shown. (r=0.93845). (J to L) Cytosolic iron imaging and quantitation in mature iNs carrying heterozygous LRRK2 mutations (J, K) as well as isogenic iNs versus controls (NIA, NIH) (L) (one-way ANOVA, Dunnett's post-hoc, N=8 biological replicates, (>800 cells per N), *p<0.05, **p<0.01, ***p<0.001, ****p<0.0001).

LRRK2 mutations cause kinase-dependent accumulation of lysosomal iron in neurons and astrocytes

The FerroOrange iron probe is reported to detect free ferrous iron in the cytosol as well as in different organelles including ER, mitochondria and endolysosomes (66–68) (Supplementary Figure 3A). Thus, the data in Figure 1 do not differentiate between cytosol and specific subcellular compartments. Given the role of lysosomes as important sites for iron mobilization regulating intracellular iron availability (69–71), and the well-established role of LRRK2 in lysosome-related pathways reported by us and others (28,29,32,72–74), we focused on evaluating lysosomal iron in LRRK2 mutant cells.

We thus employed a reported lysosomal specific ferrous iron (Fe^{2+}) probe (HMRhoNox-M) (75) to assess relative lysosomal Fe^{2+} levels across iPSCs, NGN2-induced neurons (iNs) and induced-astrocytes (iAs) (59) using high-content imaging and super-resolution microscopy (Figure 2). iAs were generated by viral delivery of doxycycline-inducible expression of SOX9 and NFIB (59). The expression of astrocytic markers and LRRK2 was confirmed at ~21 days post-induction *in vitro* (Supplementary Figure 2). We first validated the lysosomal specificity of HMRhoNox-M by comparing its staining pattern to Lamp1-emGFP localization (Figure 2A). In both iPSC-derived human neurons and astrocytes (Figure 2A), HMRhoNox-M signal was enriched within Lamp1-emGFP positive structures, supporting its preferential localization to lysosomes. Quantification of HMRhoNox-M signal in iPSCs carrying heterozygous LRRK2

mutations revealed an increase in R1441C, Y1699C and G2019S LRRK2 mutant lines compared to isogenic WT controls (Figure 2B, C). The LRRK2 mutation-driven increase in lysosomal iron as detected by HMRhoNox-M was likewise observed in differentiated iNs (Figure 2D, E) and astrocytes (Figure 2F, G) generated from these parental isogenic iPSCs.

Notably, not all HMRhoNox-M-positive puncta overlapped with Lamp1-emGFP-labeled structures, particularly in astrocytes (Figure 2A), which could reflect incomplete labeling of acidic lysosomal compartments by the Lamp1 fusion protein (76). To address this possibility directly, we performed complementary analyses using LysoTracker, which labels acidic lysosomes independently of exogenous Lamp1 expression (Figure 2F; Supplementary Figure 3). Using this approach, HMRhoNox-M showed strong colocalization with LysoTracker-positive compartments (Supplementary Figure 3A). Quantification of HMRhoNox-M selectively within LysoTracker-segmented lysosomes (Figure 2H, I) recapitulated the genotype-dependent increases observed using a whole-cell mask-based analysis (Figure 2G, H). Finally, to exclude the possibility that differences in lysosomal Fe^{2+} levels reflected changes in lysosome abundance or morphology rather than iron content per organelle, we quantified lysosome number and size across the isogenic lines. No significant differences in these parameters were observed in heterozygous LRRK2 mutant iPSCs (Supplementary Figure 3B-E), indicating that elevated HMRhoNox-M signal reflects increased lysosomal iron load rather than altered lysosomal biogenesis or expansion.

Given that LRRK2 can localize to lysosomal membranes and that lysosomal position has been reported to correlate with LRRK2 kinase activity toward Rab GTPases (77), we next examined whether iron accumulation exhibited spatial heterogeneity within the lysosomal network. Quantitative analysis revealed that the increase in lysosomal iron content in R1441C iAs was more pronounced in the perinuclear compared to the peripheral lysosomes and that this increased iron load was preferentially associated with smaller lysosomes ($< 3\ \mu m^3$) (Supplementary Figure 3F, G, H). These data are consistent with perinuclear lysosomes being sites of active LRRK2 signaling (77), as demonstrated by work from us and others showing LRRK2-dependent effects on lysosomal function and proteolytic activity (26,56,78,79).

To determine whether the increase in lysosomal iron observed in LRRK2 mutant iAs is dependent on LRRK2 kinase activity, iAs were treated with MLi-2 for 7 days prior to analysis (Figure 2J). LRRK2 inhibition reduced lysosomal iron levels in all mutant lines but not WT, with partial rescue in the R1441C and Y1699C lines and complete rescue in the G2019S line (Figure

2J). Effective inhibition of endogenous LRRK2 kinase activity was validated in parallel iPSC cultures by assessing Rab10 phosphorylation at Threonine 73, which was elevated in R1441C iPSCs and robustly reduced following acute MLi-2 (2 hrs) treatment (Supplementary Figure 4A, B). To assess the selectivity of MLi-2 on LRRK2-mediated effects on iron homeostasis, LRRK2 KO iPSCs were treated with vehicle or MLi-2 for either acute (2 hrs) or prolonged (7 day) durations and cytosolic and lysosomal iron levels were assessed. MLi-2 had no effect on iron levels in LRRK2 KO cells (Supplementary Figure 4C-F), indicating that MLi-2 as employed here does not possess off-target effects with respect to iron homeostasis. Together, these results provide evidence that lysosomal iron levels are increased by a series of pathogenic LRRK2 mutations in a kinase-dependent manner.

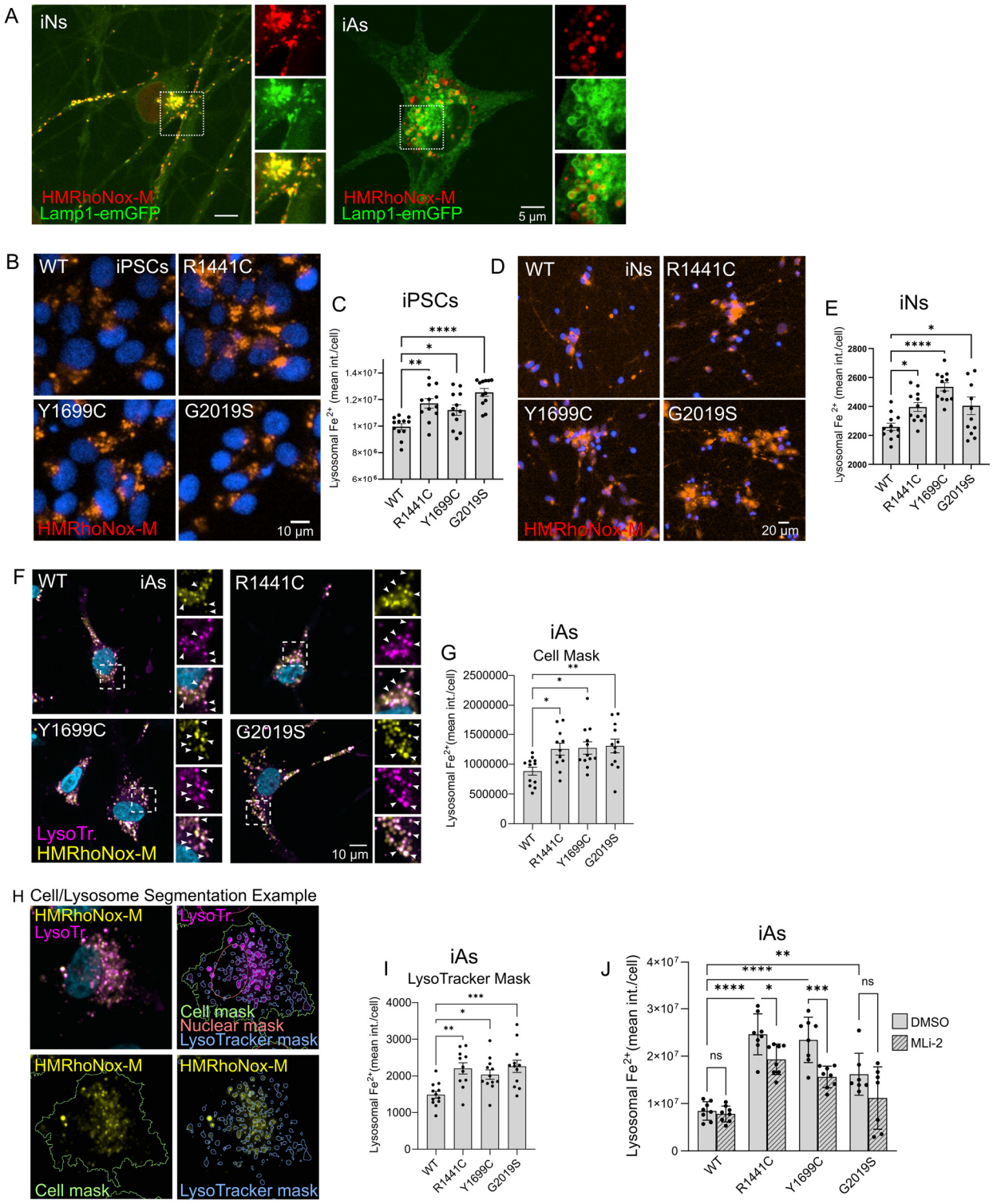

Figure 2. LRRK2 mutations increase lysosomal iron in isogenic neurons and astrocytes. (A). Representative images of lysosomal iron (HMRhoNox-M) and Lamp1-emGFP by super-resolution confocal microscopy in iNs and iAs. Lysosomal iron imaging and quantitation in heterozygous LRRK2 mutant isogenic iPSCs (B, C), isogenic iNs (D, E), and isogenic iAs (F, G). Quantification was performed using a whole-cell mask to capture total cellular HMRhoNox-M signal (one-way ANOVA, Dunnett's post-hoc, N=8 biological replicates, (>800 cells per N), *p<0.05, **p<0.01, ***p<0.001, ****p<0.0001). (H) Representative images illustrating LysoTracker-based segmentation of acidic lysosomal compartments and corresponding detection

of lysosomal iron using HMRhoNox-M. Cell, nuclear, and LysoTracker masks used for analysis are shown. (I) Quantification of HMRhoNox-M signal specifically within LysoTracker-segmented lysosomes in isogenic iAs, demonstrating genotype-dependent increases in lysosomal iron that recapitulate those observed using whole-cell mask-based quantification. Data are shown as mean ± SEM (one-way ANOVA with Dunnett's post hoc test). (J) Lysosomal iron quantitation in iAs following treatment with MLi-2 in culture (100nM, 7 days) (two-way ANOVA, Tukey's post-hoc; N=8 biological replicates (>800 cells per N), Genotype ****p=0.0001, Treatment ****p<0.0001, Interaction p=0.0844).

Ferritin levels are dysregulated in isogenic LRRK2 mutant iPSCs

Altered cytosolic and lysosomal iron demonstrate an impairment in how cells regulate their iron levels and distribution, so we further evaluated expression of key proteins involved in these processes. Iron uptake, transport, and storage are finely regulated at the post-transcriptional level by the iron regulatory protein (IRP) and iron-responsive element (IRE) signaling pathways (80). IRP1 and IRP2 are RNA-binding proteins that interact with IREs located within the untranslated regions of specific mRNAs, to modulate iron homeostasis. These interactions repress ferritin (both FTH1 and FTL) and FPN mRNA translation while stabilizing TfR mRNA (81–83). In proliferating iPSCs cultured without iron supplements, we observed an increase in total FTH1 and FTL levels in G2019S LRRK2 cells compared to isogenic WT controls, while R1441C LRRK2 iPSCs showed a trend of lower FTH1 (Figure 3A, B, C). Consistent with an IRP-mediated loss of translational repression of ferritin heavy and light chains, G2019S iPSCs also had lower basal TfR1 levels as compared to WT (Figure 3A, D). We therefore directly measured IRP1 and IRP2 levels and activity in these LRRK2 mutants. We observed a trend of downregulation of IRP1 in the ROC-COR domain mutants that reached significance in Y1699C iPSCs, supporting impairment in IRP1 signaling (Figure 3A, E). Separately, the G2019S iPSCs showed lower IRP2 expression levels with the ROC-COR domain mutants showing a trend toward decrease (Figure 3F). To evaluate IRE-binding activities of IRP1 and IRP2, we used a biotinylated-IRE probe to separate IRE-binding IRPs from cell lysates and analyzed by immunoblotting, as before (63). The IRE-binding activity of IRP1 was lower in G2019S iPSCs compared to the isogenic WT (Figure 3G), as were IRP2 protein levels and IRE-binding activity (Figure 3A).

IRP1 activity is regulated by intracellular iron levels but can also be influenced by Fe-S cluster biogenesis as it requires a 4Fe-4S cluster to function as a cytosolic aconitase (81,84). Loss of the Fe-S cluster, under iron deficient conditions, shifts IRP1 to its IRE-binding form. In contrast, IRP2, does not coordinate an Fe-S cluster, and cellular iron availability is directly reflected by IRP2 protein levels, which increase when iron is scarce and decrease through degradation when iron is sufficient. To evaluate a potential effect of iron dyshomeostasis on mitochondrial

function, we assayed levels of mitochondrial Fe-S-containing subunits (Supplementary Figure 5), noting no differences in basal levels of UQCRFS1 (Fe-S subunit of complex III), and SDHB (Fe-S subunit of complex II). While our data suggests a mild effect of LRRK2 mutations on IRP IRE-binding activities, we observe significant effects on ferritin levels, suggesting that separate mechanisms on ferritin homeostasis may be at play.

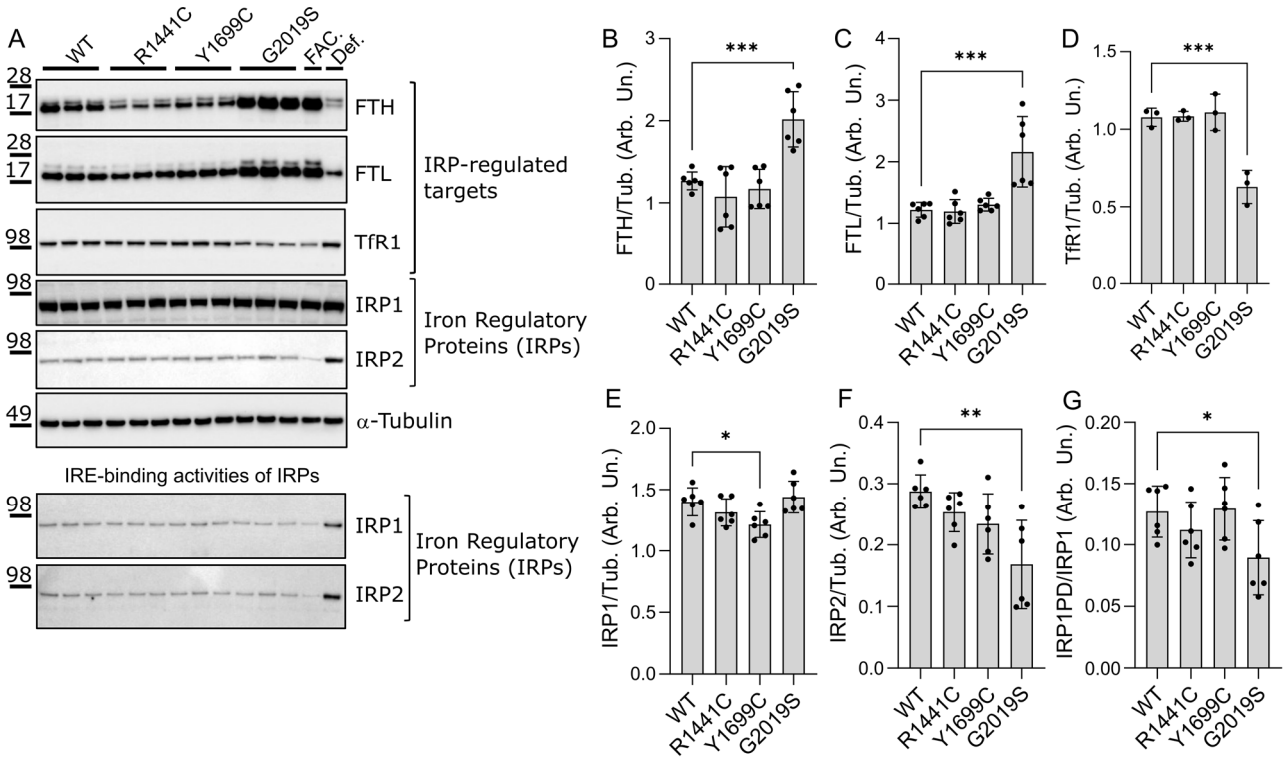

Figure 3. Ferritin heavy chain is dysregulated in isogenic LRRK2 mutant iPSCs. (A-F) Western blot analysis of IRPs (IRP1, IRP2) and IRP-regulated proteins (FTH1, FTL, TfR1) in isogenic LRRK2 mutant iPSCs. (A bottom panel, G) Western blot of IRE-bound IRP1 in isogenic LRRK2 mutant iPSCs and quantitation of IRE-binding. (one-way ANOVA, Dunnett's post-hoc, N=6 biological replicates, *p<0.05, **p<0.01, ***p<0.001).

LRRK2-Rab8a signaling controls cellular iron homeostasis

Phosphorylation of Rab GTPases by LRRK2 locks the molecules in an inactive state affecting their function (32,36,56,85). We previously showed that LRRK2-driven phosphorylation of Rab8a impairs its function in TfR trafficking, linking LRRK2 to iron homeostasis (32). Furthermore, we demonstrated that Rab8a and Rab10 knockouts (KO) produce distinct phenotypes in lysosomal integrity and PD-pathology related proteostasis (56). To test whether genetic inactivation of either of these Rab proteins is sufficient to drive dysregulation of cellular iron levels, we used CRISPR/Cas9 gene editing to generate Rab8a KO and Rab10 KO iPSCs (56) and HEK293 cells (Supplementary Figure 6), and assayed cellular iron load alongside matched isogenic controls. Using the FerroOrange probe to quantify labile cytosolic Fe^{2+} iron, we found that Rab8a but not Rab10 KO iNs showed an increase in free iron compared to isogenic WT controls, phenocopying the increase observed in mutant LRRK2 cells (Figure 4A. B). To determine whether Rab8a deficiency is causative for this phenotype, we next tested whether re-expression of Rab8a could restore iron homeostasis. Expression of exogenous GFP-Rab8a in Rab8a KO iPSCs significantly reduced FerroOrange signal, normalizing labile cytosolic Fe^{2+} iron levels toward those observed in WT cells (Figure 4C, D). These findings demonstrate that Rab8a loss is sufficient to increase labile cytosolic Fe^{2+} iron levels and that this phenotype is reversible upon Rab8a reintroduction. Notably, this increase in labile iron was specific to Rab8a loss, as Rab10 deficiency resulted in a divergent phenotype in iPSCs and HEK293 cells, supporting non-redundant roles for LRRK2-regulated Rab GTPases in iron homeostasis (Supplementary Figure 7).

To further assess how Rab8a and Rab10 deficiency influence cellular iron handling, we examined iron-related protein expression in Rab8a and Rab10 KO HEK293 cells under basal conditions and following overnight exposure to 150 µM ferric ammonium citrate (FAC). Rab8a KO cells exhibited elevated basal FTH1 levels compared to WT and Rab10 KO cells but showed a blunted FTH1 induction following FAC treatment (Supplementary Figure 7). In contrast, Rab10 KO cells displayed a robust increase in FTH1 upon iron overload. Basal TfR1 levels were increased in Rab10 KO cells, while both Rab KO lines exhibited a greater reduction in TfR1 expression following FAC treatment relative to WT. Consistent with these protein changes, Rab8a KO cells accumulated higher levels of labile iron under iron overload conditions, which was reversed by iron chelation. Together, these data further support Rab8a loss as a key driver of cellular iron accumulation; while highlighting that not all LRRK2-regulated Rab GTPases exert equivalent effects on iron-handling pathways.

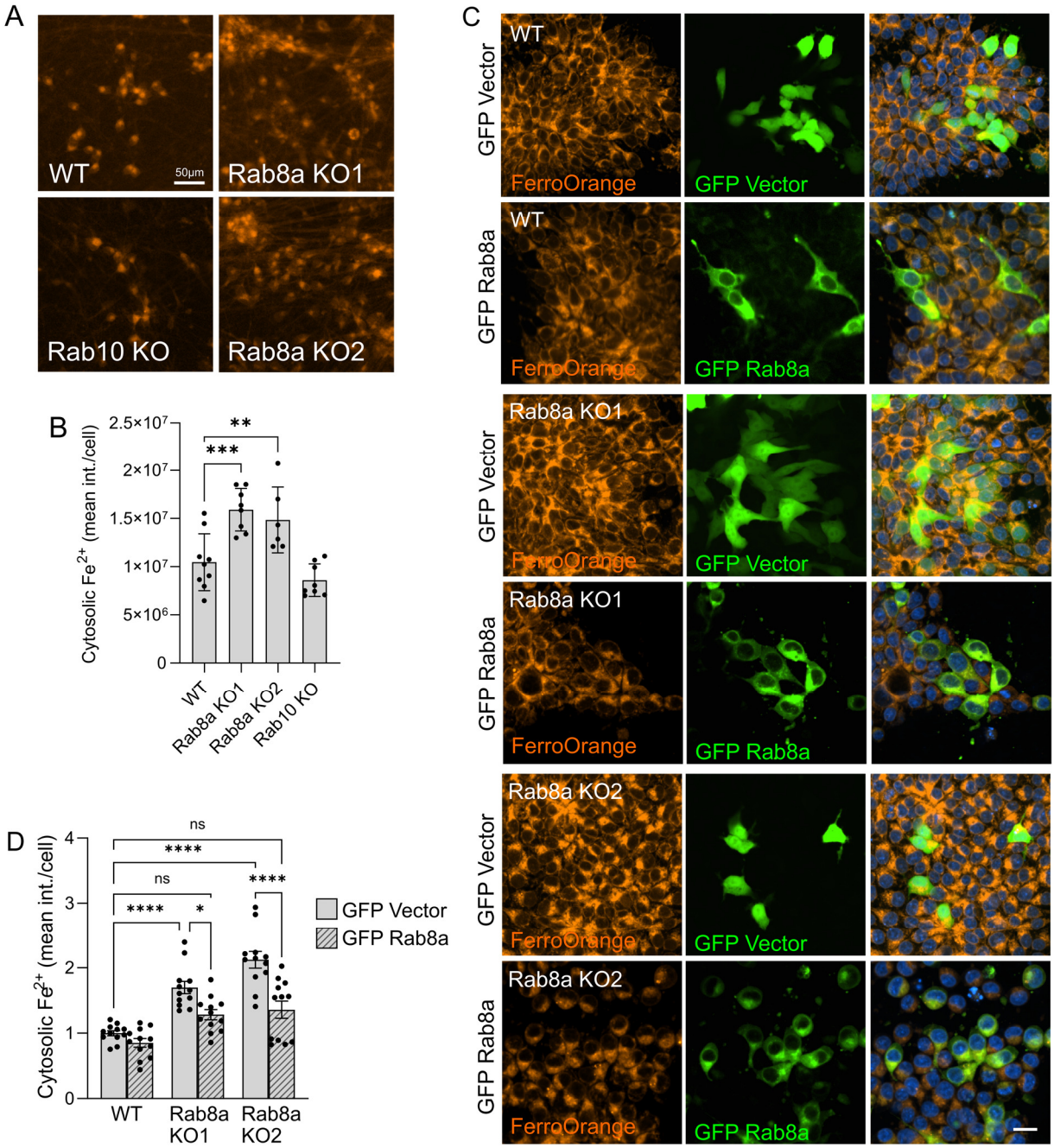

Figure 4. Knockout of the LRRK2 substrate Rab8a dysregulates cellular iron. (A, B) Imaging of cytosolic free Fe^{2+} iron and quantitation of iron levels in isogenic WT, Rab8a KO and Rab10 KO iNs by high-content imaging (one-way ANOVA, Dunnett's post-hoc, N>6 biological replicates, *p<0.05, **p<0.01, ***p<0.001, ****p<0.0001). (C, D) Representative images and quantitation of free cytosolic iron staining in WT and Rab8a KO iPSCs expressing either GFP control vector or GFP-Rab8a (two-way ANOVA, Tukey post-hoc; N=12 biological replicates (>800 cells per N), Genotype ****p<0.0001, cDNA ****p<0.0001, Interaction **p=0.0073).

The LRRK2-dependent increase in lysosomal Fe^{2+} iron was the most consistent phenotype across all pathogenic mutations and cell types analyzed. Since LRRK2 mutations are hypothesized to inactivate Rab substrates, we examined whether exogenous Rab8a over-expression could overcome this effect in R1441C LRRK2 mutant iPSCs. WT and R1441C iPSCs were transiently transfected to express either GFP or GFP-Rab8a and lysosomal iron was quantified in positively transfected cells. GFP-Rab8a expression in WT iPSCs resulted in a minor reduction in iron that did not reach statistically significant deviation from the GFP control. R1441C iPSCs transfected with GFP showed increased lysosomal iron compared to WT cells, as expected. However, expression of GFP-Rab8a in R1441C iPSCs significantly reduced lysosomal iron levels to those comparable to WT (Figure 5A-B). Collectively, these data identify Rab8a as a critical downstream effector of LRRK2-dependent iron dyshomeostasis and demonstrate that restoration of Rab8a activity is sufficient to rescue iron phenotypes associated with LRRK2 mutations.

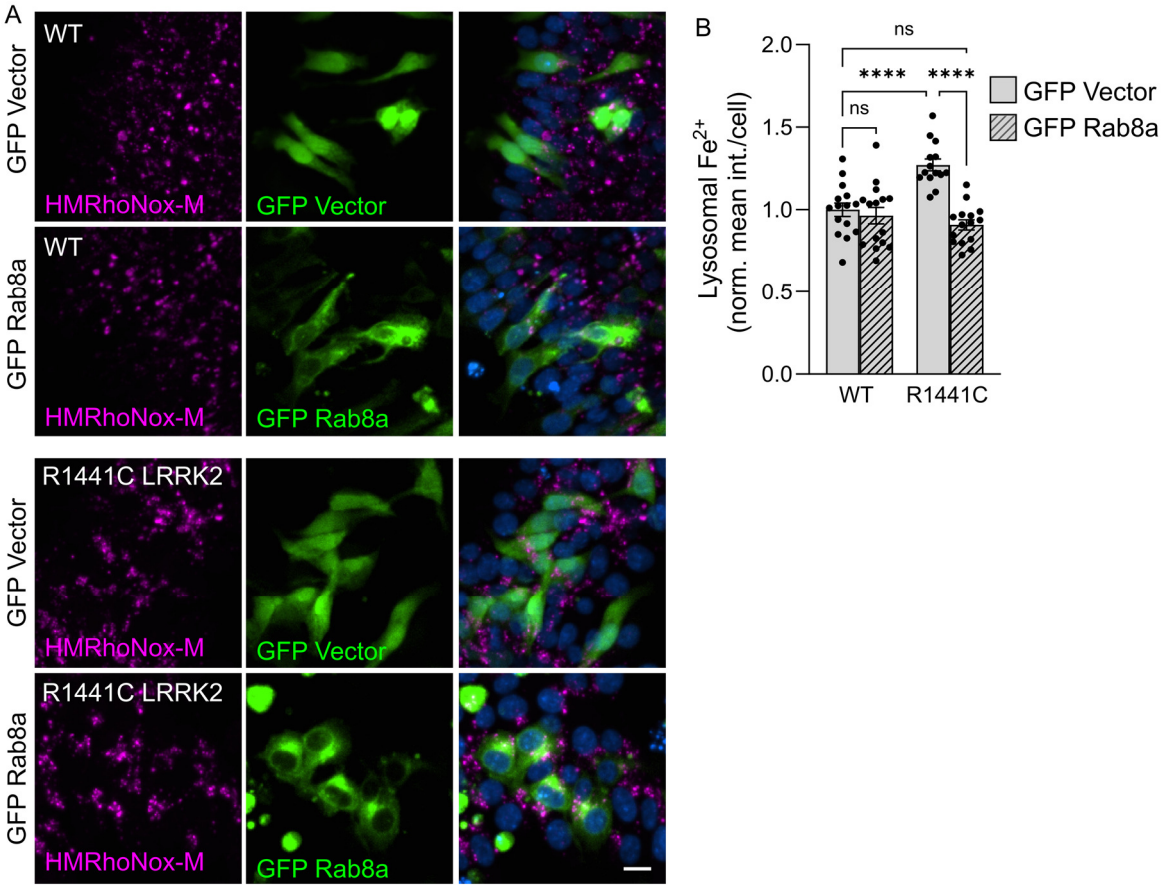

Figure 5. Exogenous Rab8a expression normalizes lysosomal iron levels in R1441C LRRK2 iPSCs. (A, B) Representative images and quantitation of lysosomal iron in WT and R1441C LRRK2 iPSCs expressing either GFP control vector or GFP-Rab8a. (two-way ANOVA, Tukey post-hoc; N=15 biological replicates (>800 cells per N), Genotype p=0.0096, cDNA ****p<0.0001, Interaction ***p=0.0002).

Iron chelation and LRRK2 inhibition protect against LRRK2-driven oxidative stress and lipid peroxidation

Ferroptosis, the process of iron-mediated lipid peroxidation and cell death, is an emerging pathogenetic mechanism of interest in the neurodegeneration in PD (20,86–88). Iron catalyzes the conversion of hydrogen peroxide to more reactive free radicals via the Fenton reaction thereby promoting oxidative injury. Ferroptosis in neurodegeneration involves the simultaneous accumulation of brain iron and lipid peroxidation, which trigger a cascade of pathologic events including inflammation, myelin sheath degeneration, glial dysregulation and cell death (89). LRRK2 mutations have been linked to increased ROS (50,51) and ferroptosis signaling (90,91) in different model systems but the mechanism by which LRRK2 signaling leads to increased cell stress remains largely unclear. Here, we examined whether dysregulated lysosomal iron in LRRK2 mutant neurons contributes to oxidative stress and downstream lipid peroxidation. Compared to isogenic WT controls, all three LRRK2 mutations led to increased lysosomal iron in differentiated iNs (Figure 6A, B). As expected, the iron chelator deferoxamine (100 µM; 16 hours) significantly reduced lysosomal iron levels below control in all cells (Figure 6A, B). Assessment of cytoplasmic ROS using CellROX revealed a genotype-dependent increase in oxidative stress in heterozygous LRRK2 mutant neurons, which was reduced by deferoxamine treatment, consistent with its ability to chelate iron in the media (Figure 6C, D). We similarly assessed lipid peroxidation with Liperfluo, which produces a prominent punctate, vesicular pattern by confocal microscopy (Supplementary Figure 8A) (92), and used erastin, a ferroptosis inducer as a positive control (Supplementary Figure 8B, C) (93–96). All three pathogenic mutations in LRRK2 significantly increased lipid peroxidation levels in iNs, which was likewise attenuated by iron chelation with deferoxamine (Figure 6E, F). Similarly, at basal conditions in proliferating cells, we detected an increase in lipid peroxidation in R1441C and G2019S iPSCs compared to isogenic WT controls (Supplementary Figure 8B, C). These data are in line with recent work that places LRRK2 in a ferroptosis pathway and highlight lipid peroxidation as a relevant mechanism in LRRK2 signaling (90,91). Together, these findings demonstrate that pathogenic LRRK2 mutations promote iron-dependent oxidative stress and lipid peroxidation in neurons, consistent with a pro-ferroptosis phenotype.

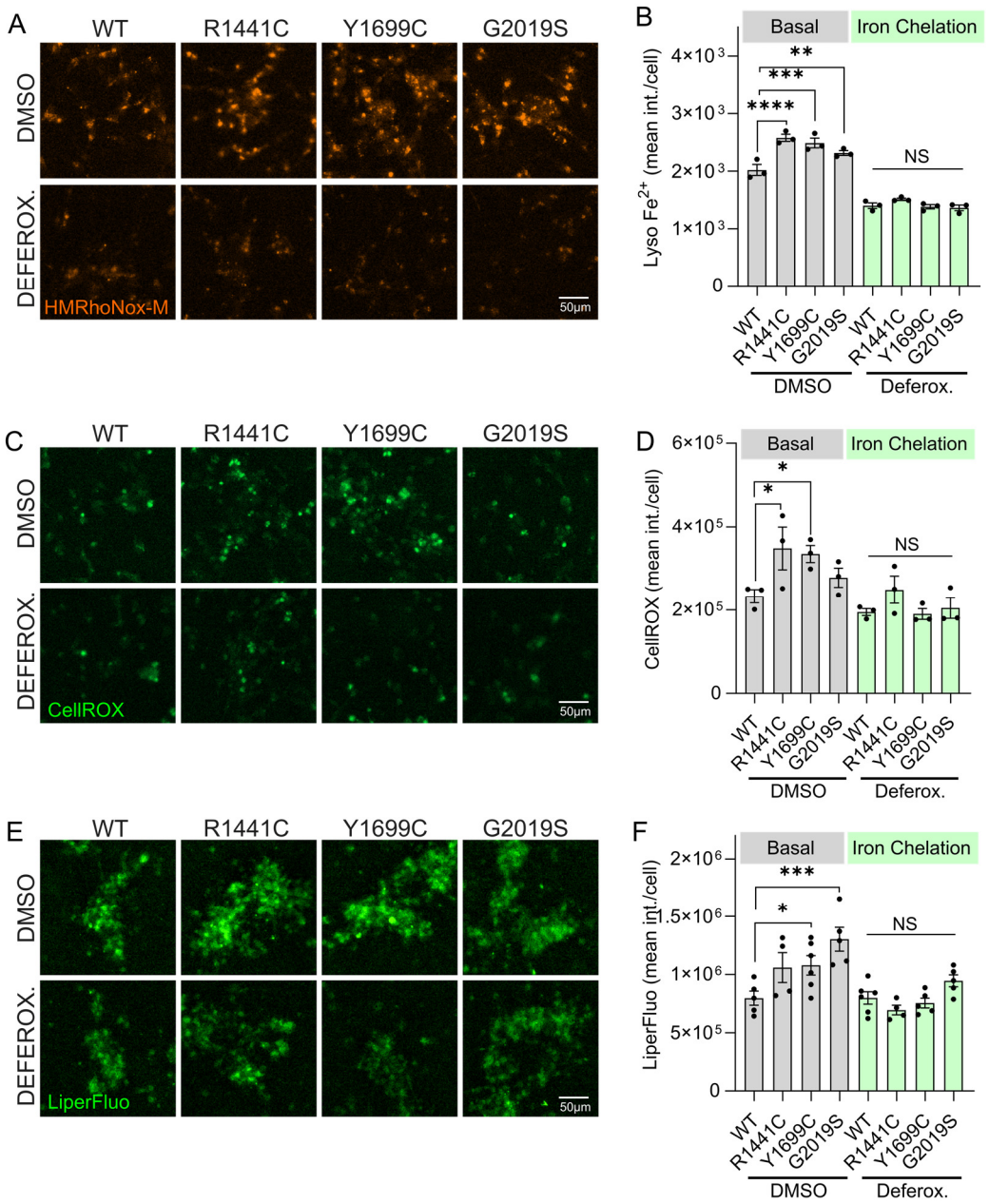

Figure 6. Iron chelation protects against LRRK2-driven ROS accumulation and ferroptosis. (A, B) High-content imaging and quantitation of lysosomal iron content (HMRhoNox-M) in iNs carrying heterozygous LRRK2 mutations versus isogenic WT controls, following treatment with 100 µM deferoxamine (16 hours) in normal media. (C, D) High-content imaging and quantitation of CellROX dye in LRRK2 mutant iNs. (E, F) Lipid peroxidation imaging (Liperfluo) and quantitation in iNs. (HMRhoNox-M: two-way ANOVA, Tukey post-hoc; N=3 biological replicates (>800 cells per N), Genotype ***p=0.0003, Treatment ****p<0.0001, Interaction **p=0.0034; CellROX: two-way ANOVA, Tukey post-hoc; N=3 biological replicates (>800 cells per N), Genotype *p=0.02, Treatment ***p=0.0002, Interaction p=0.3923; Liperfluo: two-way ANOVA, Tukey post-hoc; N=3 biological replicates (>800 cells per N), Genotype ***p=0.0009, Treatment ****p<0.0001, Interaction *p=0.0497).

To determine whether LRRK2 kinase activity contributes directly to lipid peroxidation, we next assessed the effect of pharmacological LRRK2 inhibition using MLi-2. To assess the selectivity of this inhibitor, LRRK2 KO iPSCs were treated with vehicle or MLi-2 (100 nM) for 7 days, with fresh inhibitor applied every 48 hr. No differences in basal Liperfluo signal were observed, confirming the selectivity of MLi-2 (Supplementary Figure 8D, E). We then examined the effect of selective LRRK2 kinase inhibition on lipid peroxidation in LRRK2 mutant iNs. Treatment of mature iNs with MLi-2 significantly reduced Liperfluo signal in R1441C, Y1699C, and G2019S neurons, reducing lipid peroxidation levels toward those observed in WT controls (Figure 7A, B). These data indicate that lipid peroxidation is increased in LRRK2 mutant neurons in a kinase-dependent manner.

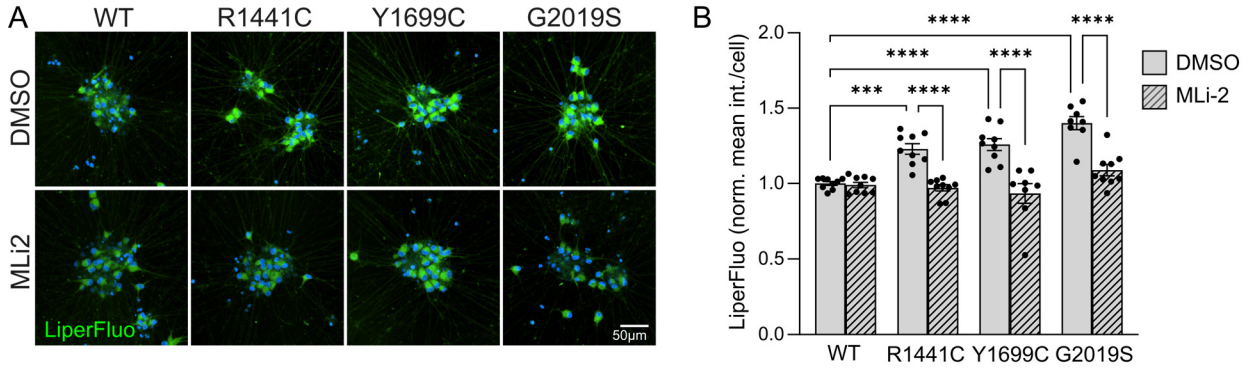

Figure 7. Selective kinase inhibition reduces lipid peroxidation in LRRK2-mutant neurons. (A, B) Representative images and quantitation of lipid peroxidation detected by Liperfluo in mature iNs expressing WT or isogenic LRRK2 variants following treatment with vehicle or MLi-2 (100 nM, 7 days) (two-way ANOVA, Tukey post-hoc; N=9 biological replicates (>800 cells per N), Genotype $p<0.0001$, Treatment $p<0.0001$, Interaction $p<0.0001$).

LRRK2 kinase-dependent iron dysregulation in human DA neurons

Given the selective vulnerability of DA neurons in PD, we next examined whether LRRK2 mutations dysregulate iron homeostasis and oxidative stress in human iPSC-derived DAs. DA neurons were generated from isogenic WT and LRRK2 mutant iPSCs using established protocols (61,62) and TH positivity was confirmed by ICC (Supplementary Figure 9A). Mature DAs carrying LRRK2 mutations were treated with the LRRK2 kinase inhibitor MLi-2 for 7 days prior to analysis. Assessment of lysosomal iron revealed a significant increase in both R1441C and Y1699C DA neurons compared to WT controls, which was rescued by MLi-2 treatment (Figure 8A, B). Subsequent lipid peroxidation analyses were focused on R1441C DA neurons, as this mutation showed robust Rab8a phosphorylation (32) and the most pronounced changes across multiple iron-related readouts examined here. R1441C DA neurons exhibited

significantly increased lipid peroxidation compared to WT controls (Figure 8C, D). Importantly, the LRRK2 mutation-driven increase in lipid peroxidation was significantly reduced by selective LRRK2 kinase inhibition in DA neurons, with no effect in WT DA neurons (Figure 8C, D). To verify the selectivity of MLi-2 for LRRK2 kinase activity in DA neurons, as previously established in iPSCs (Supplementary Figure 8), LRRK2 KO DA neurons were treated with vehicle or 100 nM MLi-2 for 7 days. MLi-2 had no effect on Liperfluo signal in the LRRK2 KO DA neurons, confirming its specificity for this measure in these neurons (Supplementary Figure 9B, C). Together, these data demonstrate that pathogenic LRRK2 mutations promote lysosomal iron accumulation and lipid peroxidation in human DA neurons, with both phenotypes dependent on a pathogenic increase in LRRK2 kinase activity.

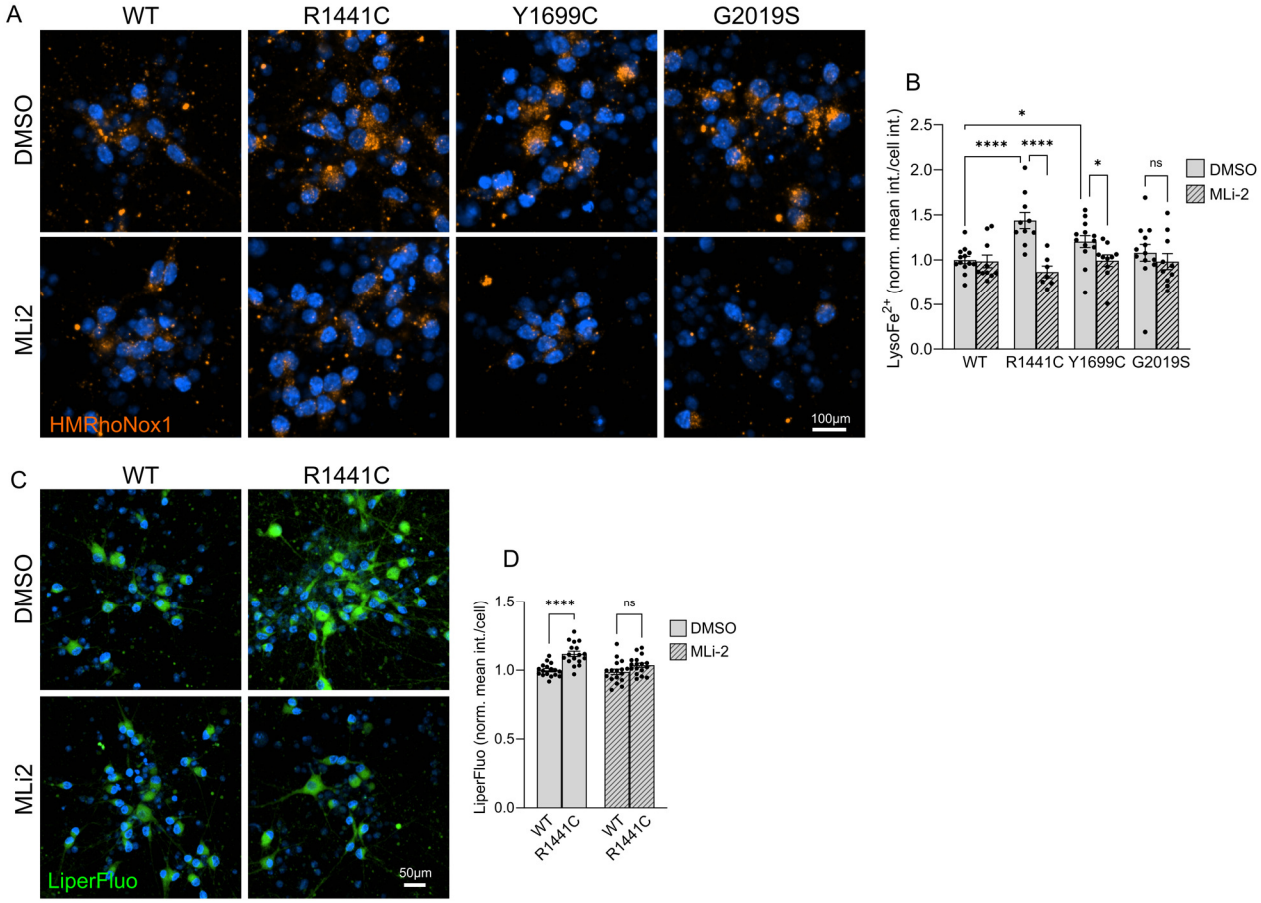

Figure 8. LRRK2 kinase inhibition modulates iron and lipid peroxidation in human dopaminergic neurons. (A, B) Representative images and quantitation of lysosomal iron (HMRhoNox-M) in mature human iPSC-derived DA neurons of the indicated genotypes following treatment with vehicle (DMSO) or MLi-2 (100 nM, 7 days) (two-way ANOVA, Tukey post-hoc; N>10 biological replicates (>800 cells per N), Genotype p=0.1953, Treatment p<0.0001, Interaction p=0.0061). (C, D) Representative images and quantitation of lipid peroxidation (Liperfluo) in WT and heterozygous R1441C DA neurons following treatment with DMSO or MLi-2. (two-way ANOVA, Tukey post-hoc; N=15 biological replicates (>800 cells per N), Genotype p<0.0001, Treatment p=0.0148, Interaction p=0.1211).

Discussion

The pathological deposition of iron in the PD brain has been widely documented for over three decades, with early histochemical studies identifying iron accumulation in the substantia nigra of post-mortem PD tissue (97,98), and subsequent MRI and spectroscopic studies confirming region-specific iron overload *in vivo* (9,99,100). However, the mechanisms by which genetic risk factors may contribute to intracellular iron mismanagement have remained poorly defined. In this study we show that PD-linked LRRK2 mutations disrupt iron handling in human iPSCs, neurons, and astrocytes, with a striking and convergent increase in lysosomal ferrous iron. This iron accumulation is kinase-dependent and reversible, implicating chronic aberrant LRRK2 signaling in the misregulation of vesicular iron storage. By integrating imaging, biochemical assays, and isogenic models, we report a role for Rab8a in LRRK2-driven iron defects and demonstrate that LRRK2 mutations may enhance iron-driven oxidative stress in human DA neurons. These findings provide a mechanistic link between LRRK2 activity and iron toxicity, offering new insight into the neuronal vulnerabilities that may drive neurodegeneration in PD.

Most pathogenic LRRK2 mutations cluster within the kinase and the Roc-COR tandem domains of the protein, and all are thought to augment the kinase activity of LRRK2 towards a subset of Rab GTPases (34). Rab GTPases control many aspects of intracellular vesicle trafficking by acting as regulatable switches that recruit effector molecules to distinct intracellular membranes (36,101). We and others have shown that phosphorylation of Rab GTPases by mutant LRRK2, including Rab8a and Rab10, interferes with their function and alters endolysosomal dynamics (26,28,32,34,35,102–104). Furthermore, it has been reported that recruitment of LRRK2 to damaged lysosomes, along with Rab8a and Rab10, affects lysosomal integrity (28,32,72). Studies have shown divergent effects of Rab8a and Rab10 in cilliogenesis (105) and we recently reported divergent lysosomal phenotypes between Rab8a KO and Rab10 KO cells (56). Here, we extend this work by demonstrating that loss of Rab8a but not Rab10 partially mimics aspects of iron impairment observed in LRRK2 mutant cells, including upregulation of labile cellular iron and ferritin. Importantly, exogenous Rab8a expression rescued lysosomal iron accumulation in R1441C LRRK2 mutant cells, providing direct evidence that impaired Rab8a activity contributes causally to iron misregulation downstream of pathogenic LRRK2 signaling. Together, these findings define a novel Rab8a-dependent pathway linking LRRK2 kinase activity to intracellular iron handling, potentially through its role in transferrin receptor trafficking

and lysosomal function (32,40). The focus on Rab8a is especially interesting given its additional relationship with PINK1 and α-synuclein biology (106–108).

Lysosomes serve as crucial hubs for iron storage and availability (70,71). Physiologic delivery of iron to cells is primarily mediated by transferrin, which binds ferric iron in the extracellular environment and is internalized through clathrin-dependent endocytosis via the transferrin receptor, while non-transferrin bound iron (NTBI) uptake can play a role in iron uptake associated with systemic iron overload or trauma (109). Within endolysosomes, the acidic environment facilitates the release of iron from transferrin and endolysosomal ferrireductases reduce Fe^{3+} to Fe^{2+}, allowing iron exit into the cytoplasm through DMT1. This endolysosomal acidification step is critical for iron release and trafficking, and its disruption has been linked to cellular iron deficiency, mitochondrial dysfunction, and inflammation (71,110,111). In fact, inhibition of the lysosomal v-ATPase triggers cellular iron dyshomeostasis, resulting in impaired mitochondrial function and non-apoptotic cell death *in vivo* (110). Here, by using a lysosomal-specific iron probe we found that LRRK2 mutations lead to increased lysosomal ferrous iron content, an effect observed in both terminally differentiated neurons and astrocytes. These data, together with previous reports linking LRRK2 to lysosomal function (28,32,72), and specifically intralumenal pH (26,79), suggest that LRRK2 mutations disrupt normal lysosomal iron handling by altering lysosomal homeostasis. We found that perinuclear lysosomes have a pronounced increase in ferrous iron in LRRK2 mutant astrocytes compared to peripheral lysosomes. Studies have shown that perinuclear lysosomes have lower luminal pH and higher protease activity compared to distal ones (78). Lysosomal positioning correlates with LRRK2 activity towards Rab GTPases with perinuclear lysosomes harboring enhanced kinase-driven Rab signaling (77). We and others have reported dysregulation of lysosomal acidification by mutant LRRK2 in different cellular models (26,31,79,112,113). It is plausible that altered acidification impacts iron mobilization from the lysosome and thus alters overall cellular iron content and availability in the context of LRRK2 mutations.

Iron-induced oxidative stress is a well-documented contributor to neurodegeneration, and our results support a role for LRRK2 mutations in exacerbating this process in DA neurons. Iron-induced cell death, termed ferroptosis, has emerged as a key mechanism contributing to oxidative damage and neuronal loss in PD models (20,86–88). The convergence of aberrant brain iron and lipid peroxidation initiates downstream pathology marked by inflammation, glial dysfunction, demyelination, and ultimately neuronal death (89). Here, we observed increased lipid peroxidation and ROS levels in mutant LRRK2 DA neurons and glutamatergic iNs, which were reversed by iron chelation and LRRK2 inhibition. LRRK2 has been linked to ROS

accumulation in different models (50–52), while a recent study reported an effect of LRRK2 mutations in NOX2 activity that in turn has been linked to ferroptosis (51,114,115). Furthermore, studies have linked G2019S LRRK2 with heightened oxidative stress vulnerability in human iPSC-derived DA neurons (116), while more recently, *in vivo* data suggested age-dependent oxidative stress and mitochondrial dysfunction in the SNc of R1441G LRRK2 BAC transgenic mice (117). These data are consistent with mitochondrial abnormalities and dopaminergic alterations reported in G2019S knockin mice (118). It is plausible that dysregulation of the labile and lysosomal iron pools by LRRK2 mutations contributes to the reported effects of LRRK2 on cellular ROS. The lysosomal membrane is exposed to redox-active iron and is an initial target of intracellular oxidant damage, with studies reporting a protective role for intralysosomal iron chelation against ROS damage (119). A recent study identified the lysosomal protein prosaposin as an important regulator of lipid peroxidation and neuronal ROS (92). LRRK2 signaling has been linked to prosaposin function *in vitro* and *in vivo*, highlighting a potential functional interaction that could mediate ferroptosis signaling in this context (120,121). What remains to be established is whether dysregulation of lysosomal Fe^{2+} levels by mutant LRRK2 solely drives cellular ROS damage, or whether aberrant transport of endolysosomal iron to the labile or mitochondrial iron pools also contribute pathologic effects. The finding that deferoxamine attenuated both ROS and lysosomal iron content further strengthens the connection between lysosomal iron mismanagement and oxidative stress in PD-relevant cell types. Ferroptosis inhibitors have shown promise in mitigating neurodegeneration in cell and in *in vivo* preclinical models (20,89,122) Thus, targeting lysosomal LRRK2-mediated iron dysregulation may represent a viable therapeutic strategy.

Cellular iron homeostasis is tightly regulated at the post-transcriptional level by IRPs, which bind to IREs in target mRNAs to control the expression of key iron-handling proteins (80,81,83,84). In our models, ferritin levels were particularly dysregulated in G2019S LRRK2 lines, while IRP1/2 activity showed genotype-specific variation. Notably, cytosolic ferritin levels did not correlate strictly with IRP binding activity, implying that lysosomal dysfunction and impaired ferritin turnover may dominate ferritin regulation in the context of mutant LRRK2 signaling. Interestingly, G2019S showed stronger effects on IRP/ferritin regulation compared to R1441C and Y1699C, but a less convergent effect on iron levels across different cell types. A recent study reported impaired regulation of the ferritinophagy adaptor NCOA4 in G2019 LRRK2 macrophages in a yet-to-be defined kinase-independent manner (123). Previously, we reported elevated levels of ferritin in the brain of G2019S LRRK2 mice, following proinflammatory stimulation (32). It is possible that disruption of ferritinophagy in the context of G2019S LRRK2

underlies altered ferritin levels and mobilization, while ROC-COR domain mutations may impact iron homeostasis via partially divergent mechanisms.

Our data reveal that LRRK2 mutations drive lysosomal iron accumulation in both neurons and astrocytes, supporting a model in which iron dysregulation arises through both cell-autonomous and non-cell-autonomous mechanisms. Astrocytes are essential regulators of brain iron homeostasis, not only by sequestering and buffering excess iron, but also by modulating iron availability at synaptic interfaces through secretion of factors that support neuronal iron uptake (41,42,45–47,124). By shaping the extracellular iron landscape, astrocytes maintain appropriately low synaptic levels and influence neuronal redox balance (45,124). Astrocytes are relevant to LRRK2 biology as they express high levels of LRRK2 (31,125,126), and their cytokine profile is modulated by LRRK2 kinase activity (43,44,48). The increase in lysosomal ferrous iron observed in LRRK2 mutant astrocytes suggests a failure of astrocytic iron buffering capacity, that in an *in vivo* setting would translate into alterations of the synaptic iron microenvironment. In parallel, the accumulation of lysosomal iron in LRRK2 mutant neurons reflects intrinsic defects in iron trafficking and storage, further sensitizing neurons to oxidative injury and ferroptosis. These findings highlight the potential for a dual contribution of LRRK2 to neurodegeneration: through direct, cell-autonomous disruption of neuronal iron handling, and indirectly by impairing astrocyte-mediated regulation of extracellular iron homeostasis.

Based on our current findings from human iPSC-derived models, further work will be needed to confirm whether similar lysosomal iron redistribution occurs *in vivo* in preclinical models where we and others previously reported effects on global iron pathways (32,35,127). Additionally, while iron chelation and LRRK2 inhibition both rescued aspects of the phenotype, a dual therapeutic strategy remains to be tested in preclinical models. Importantly, iron chelation is an effective treatment in Neurodegeneration with Brain Iron Accumulation that often includes parkinsonism symptoms (128–131), but recent clinical trials in PD failed (132) suggesting that targeting precise iron pathways pertaining ferroptosis signaling, in combination with other strategies, in the brain rather than systemic chelation may be considered for future therapeutic efforts for altering disease progression.

Conclusion

Our findings identify lysosomal iron dysregulation as a key downstream consequence of pathogenic LRRK2 activity in PD. We demonstrate that LRRK2 regulates neuronal and glial iron

homeostasis through effects on lysosomal iron trafficking, and that disruption of this pathway leads to redox imbalance and increased ferroptotic vulnerability. The identification of Rab8a, a protein also linked to PINK1 and α-synuclein dependent misregulation, as a critical LRRK2 substrate in this process provides a mechanistic link between LRRK2 signaling and iron biology, offering insight into how genetic and idiopathic PD may converge on a shared pathogenic pathway.

List of abbreviations

PD	Parkinson's disease
iPSC	Induced pluripotent stem cell
iNs	Induced neurons
iAs	Induced astrocytes
LRRK2	Leucine-rich repeat kinase 2
ROS	Reactive oxygen species
FAC	Ferric ammonium citrate
DEF	Deferoxamine
TfR1	Transferrin receptor 1
DMT1	Divalent metal transporter 1
Fth1	Ferritin heavy chain
Ftl	Ferritin light chain
IRP	Iron regulatory protein
IRE	Iron-responsive element
ICP-MS	Inductively coupled plasma mass spectrometry
QSM	Quantitative susceptibility mapping
PPMI	Parkinson's Progression Markers Initiative
ANOVA	Analysis of variance
WT	Wild-type
TH	Tyrosine Hydroxylase

Declarations

Ethics approval and consent to participate

Most experiments were performed using isogenic iPSC lines provided by the laboratory of Mark Cookson (National Institutes of Health) that were generated from the commercially available A18945 parental iPSC line (Thermo Fisher Scientific). Written informed consent for research was obtained from all participants in the Parkinson's Progression Markers Initiative (PPMI), a multi-center study approved by the institutional review boards at each participating site (individual IRB approval numbers are held by the originating institutions). Additional human iPSC lines were obtained from the NINDS Human Cell and Data Repository and were generated under approved institutional review board protocols with documented informed consent. All procedures involving human-derived materials were conducted in accordance with the principles of the Declaration of Helsinki.

Consent for publication

This manuscript was reviewed by the PPMI Data and Publications Committee and is permitted for publication.

Availability of data and materials

Materials and additional details can be made available by the corresponding authors upon request.

Competing interests

The authors declare that they have no competing financial interests.

Funding

This work was supported in part by the Michael J. Fox Foundation for Parkinson's Research (MJFF) grant MJFF-023425 (A.M., M.J.L.), National Institutes of Health grants NS110188 and AG082373 (M.J.L.) and AG077269 (A.M.), ES033625 (C.V) and the Intramural Research Program of the NIH, *Eunice Kennedy Shriver* National Institute of Child Health and Human Development.

Authors' contributions

Conceptualization: AM, MJL; Methodology: AM, RDB, TBD, AC, NS, AS, NM; Formal analysis and investigation: AM, RDB, TBD, AS, AC, NS, NM; Writing - original draft preparation: AM; Writing - review and editing: AM, MJL, RDB, AC, NS, NM, CDV; Funding acquisition: AM, MJL,

CDV; Resources: AM, MJL, CDV; Supervision: MJL, AM. All authors read and approved the final manuscript.

Acknowledgements

We thank Dr. Jeffrey R. Jones (CTRND, University of Florida) for helpful discussions. We thank the patients and controls who volunteered to the study and the Parkinson's Progression Markers Initiative (PPMI) for providing access to their samples and data. Data used in the preparation of this article was obtained between 03 November 2023 and 10 November 2023 from the PPMI database (www.ppmi-info.org/access-data-specimens/download-data), RRID:SCR_006431. For up-to-date information on the study, visit www.ppmi-info.org. PPMI, a public-private partnership, is funded by The Michael J. Fox Foundation for Parkinson's Research and funding partners, including 4D Pharma, AbbVie, AcureX, Allergan, Amathus Therapeutics, Aligning Science Across Parkinson's, AskBio, Avid Radiopharmaceuticals, BIAL, BioArctic, Biogen, Biohaven, BioLegend, BlueRock Therapeutics, Bristol-Myers Squibb, Calico Labs, Capsida Biotherapeutics, Celgene, Cerevel Therapeutics, Coave Therapeutics, DaCapo Brainscience, Denali, Edmond J. Safra Foundation, Eli Lilly, Gain Therapeutics, GE HealthCare, Genentech, GSK, Golub Capital, Handl Therapeutics, Insitro, Jazz Pharmaceuticals, Johnson & Johnson Innovative Medicine, Lundbeck, Merck, Meso Scale Discovery, Mission Therapeutics, Neurocrine Biosciences, Neuron23, Neuropore, Pfizer, Piramal, Prevail Therapeutics, Roche, Sanofi, Servier, Sun Pharma Advanced Research Company, Takeda, Teva, UCB, Vanqua Bio, Verily, Voyager Therapeutics, The Weston Family Foundation, and Yumanity Therapeutics.

References

1. Ayton S, Lei P. Nigral Iron Elevation Is an Invariable Feature of Parkinson's Disease and Is a Sufficient Cause of Neurodegeneration. Biomed Res Int [Internet]. 2014 [cited 2019 Jun 12];2014. Available from: https://www.ncbi.nlm.nih.gov/pmc/articles/PMC3914334/

2. Barbosa JHO, Santos AC, Tumas V, Liu M, Zheng W, Haacke EM, et al. Quantifying brain iron deposition in patients with Parkinson's disease using quantitative susceptibility mapping, R2 and R2*. Magnetic Resonance Imaging. 2015 Jun 1;33(5):559–65.

3. De Barros A, Arribarat G, Combis J, Chaynes P, Péran P. Matching ex vivo MRI With Iron Histology: Pearls and Pitfalls. Front Neuroanat. 2019 Jul 3;13:68.

4. Guan X, Lancione M, Ayton S, Dusek P, Langkammer C, Zhang M. Neuroimaging of Parkinson's disease by quantitative susceptibility mapping. NeuroImage. 2024 Apr 1;289:120547.

5. Lehéricy S, Roze E, Goizet C, Mochel F. MRI of neurodegeneration with brain iron accumulation. Current Opinion in Neurology. 2020 Aug;33(4):462.

6. Thomas GEC, Zarkali A, Ryten M, Shmueli K, Gil-Martinez AL, Leyland LA, et al. Regional brain iron and gene expression provide insights into neurodegeneration in Parkinson's disease. Brain. 2021 Jun 1;144(6):1787–98.

7. Virel A, Faergemann E, Orädd G, Strömberg I. Magnetic Resonance Imaging (MRI) to Study Striatal Iron Accumulation in a Rat Model of Parkinson's Disease. PLOS ONE. 2014 Nov 14;9(11):e112941.

8. Zecca L, Berg D, Arzberger T, Ruprecht P, Rausch WD, Musicco M, et al. In vivo detection of iron and neuromelanin by transcranial sonography: a new approach for early detection of substantia nigra damage. Mov Disord. 2005 Oct;20(10):1278–85.

9. Wallis LI, Paley MNJ, Graham JM, Grünewald RA, Wignall EL, Joy HM, et al. MRI assessment of basal ganglia iron deposition in Parkinson's disease. Journal of Magnetic Resonance Imaging. 2008;28(5):1061–7.

10. Boelmans K, Holst B, Hackius M, Finsterbusch J, Gerloff C, Fiehler J, et al. Brain iron deposition fingerprints in Parkinson's disease and progressive supranuclear palsy. Mov Disord. 2012 Mar;27(3):421–7.

11. Lee JH, Lee MS. Brain Iron Accumulation in Atypical Parkinsonian Syndromes: in vivo MRI Evidences for Distinctive Patterns. Front Neurol [Internet]. 2019 Feb 12 [cited 2025 Apr 1];10. Available from: https://www.frontiersin.org/journals/neurology/articles/10.3389/fneur.2019.00074/full

12. Lee SH, Lyoo CH, Ahn SJ, Rinne JO, Lee MS. Brain regional iron contents in progressive supranuclear palsy. Parkinsonism Relat Disord. 2017 Dec;45:28–32.

13. Wang Y, Butros SR, Shuai X, Dai Y, Chen C, Liu M, et al. Different Iron-Deposition Patterns of Multiple System Atrophy with Predominant Parkinsonism and Idiopathetic Parkinson Diseases Demonstrated by Phase-Corrected Susceptibility-Weighted Imaging. AJNR Am J Neuroradiol. 2012 Feb;33(2):266–73.

14. Mitchell T, Lehéricy S, Chiu SY, Strafella AP, Stoessl AJ, Vaillancourt DE. Emerging Neuroimaging Biomarkers Across Disease Stage in Parkinson Disease: A Review. JAMA Neurol. 2021 Oct 1;78(10):1262–72.

15. Salazar J, Mena N, Hunot S, Prigent A, Alvarez-Fischer D, Arredondo M, et al. Divalent metal transporter 1 (DMT1) contributes to neurodegeneration in animal models of Parkinson's disease. PNAS. 2008 Nov 25;105(47):18578–83.

16. Youdim MBH, Stephenson G, Ben Shachar D. Ironing iron out in Parkinson's disease and other neurodegenerative diseases with iron chelators: a lesson from 6-hydroxydopamine and iron chelators, desferal and VK-28. Ann N Y Acad Sci. 2004 Mar;1012:306–25.

17. Stockwell BR, Friedmann Angeli JP, Bayir H, Bush AI, Conrad M, Dixon SJ, et al. Ferroptosis: A Regulated Cell Death Nexus Linking Metabolism, Redox Biology, and Disease. Cell. 2017 Oct 5;171(2):273–85.

18. Hambright WS, Fonseca RS, Chen L, Na R, Ran Q. Ablation of ferroptosis regulator glutathione peroxidase 4 in forebrain neurons promotes cognitive impairment and neurodegeneration. Redox Biol. 2017 Aug;12:8–17.

19. Dixon SJ, Lemberg KM, Lamprecht MR, Skouta R, Zaitsev EM, Gleason CE, et al. Ferroptosis: an iron-dependent form of nonapoptotic cell death. Cell. 2012 May 25;149(5):1060–72.

20. Do Van B, Gouel F, Jonneaux A, Timmerman K, Gelé P, Pétrault M, et al. Ferroptosis, a newly characterized form of cell death in Parkinson's disease that is regulated by PKC. Neurobiol Dis. 2016 Oct;94:169–78.

21. Liu L, Cui Y, Chang YZ, Yu P. Ferroptosis-related factors in the substantia nigra are associated with Parkinson's disease. Sci Rep. 2023 Sep 16;13(1):15365.

22. Wen S, Aki T, Unuma K, Uemura K. Chemically Induced Models of Parkinson's Disease: History and Perspectives for the Involvement of Ferroptosis. Frontiers in Cellular Neuroscience [Internet]. 2020 [cited 2023 Jan 1];14. Available from: https://www.frontiersin.org/articles/10.3389/fncel.2020.581191

23. Zuo Y, Xie J, Li X, Li Y, Thirupathi A, Zhang J, et al. Ferritinophagy-Mediated Ferroptosis Involved in Paraquat-Induced Neurotoxicity of Dopaminergic Neurons: Implication for Neurotoxicity in PD. Oxidative Medicine and Cellular Longevity. 2021 Jul 26;2021:e9961628.

24. Tong ZB, Kim H, El Touny L, Simeonov A, Gerhold D. LUHMES Dopaminergic Neurons Are Uniquely Susceptible to Ferroptosis. Neurotox Res. 2022 Oct;40(5):1526–36.

25. Kluss JH, Mamais A, Cookson MR. LRRK2 links genetic and sporadic Parkinson's disease. Biochem Soc Trans. 2019 Apr 30;47(2):651–61.

26. Schapansky J, Khasnavis S, DeAndrade MP, Nardozzi JD, Falkson SR, Boyd JD, et al. Familial knockin mutation of LRRK2 causes lysosomal dysfunction and accumulation of endogenous insoluble α-synuclein in neurons. Neurobiol Dis. 2018 Mar;111:26–35.

27. Beilina A, Bonet-Ponce L, Kumaran R, Kordich JJ, Ishida M, Mamais A, et al. The Parkinson's Disease Protein LRRK2 Interacts with the GARP Complex to Promote Retrograde Transport to the trans-Golgi Network. Cell Rep. 2020 May 5;31(5):107614.

28. Bonet-Ponce L, Beilina A, Williamson CD, Lindberg E, Kluss JH, Saez-Atienzar S, et al. LRRK2 mediates tubulation and vesicle sorting from lysosomes. Science Advances. 2020 Nov 1;6(46):eabb2454.

29. Sanyal A, Novis HS, Gasser E, Lin S, LaVoie MJ. LRRK2 Kinase Inhibition Rescues Deficits in Lysosome Function Due to Heterozygous GBA1 Expression in Human iPSC-Derived Neurons. Front Neurosci [Internet]. 2020 May 15 [cited 2020 Jul 31];14. Available from: https://www.ncbi.nlm.nih.gov/pmc/articles/PMC7243441/

30. Biskup S, Moore DJ, Celsi F, Higashi S, West AB, Andrabi SA, et al. Localization of LRRK2 to membranous and vesicular structures in mammalian brain. Ann Neurol. 2006 Nov;60(5):557–69.

31. Henry AG, Aghamohammadzadeh S, Samaroo H, Chen Y, Mou K, Needle E, et al. Pathogenic LRRK2 mutations, through increased kinase activity, produce enlarged lysosomes with reduced degradative capacity and increase ATP13A2 expression. Human Molecular Genetics. 2015 Nov 1;24(21):6013–28.

32. Mamais A, Kluss JH, Bonet-Ponce L, Landeck N, Langston RG, Smith N, et al. Mutations in LRRK2 linked to Parkinson disease sequester Rab8a to damaged lysosomes and regulate transferrin-mediated iron uptake in microglia. PLOS Biology. 2021 Dec 16;19(12):e3001480.

33. Pyatigorskaya N, Sharman M, Corvol JC, Valabregue R, Yahia-Cherif L, Poupon F, et al. High nigral iron deposition in LRRK2 and Parkin mutation carriers using R2* relaxometry. Movement Disorders. 2015;30(8):1077–84.

34. Steger M, Tonelli F, Ito G, Davies P, Trost M, Vetter M, et al. Phosphoproteomics reveals that Parkinson's disease kinase LRRK2 regulates a subset of Rab GTPases. eLife [Internet]. 2016 Jan 29 [cited 2016 Apr 28];5. Available from: http://elifesciences.org/lookup/doi/10.7554/eLife.12813

35. Kluss JH, Mazza MC, Li Y, Manzoni C, Lewis PA, Cookson MR, et al. Preclinical modeling of chronic inhibition of the Parkinson's disease associated kinase LRRK2 reveals altered function of the endolysosomal system in vivo. Molecular Neurodegeneration. 2021 Mar 19;16(1):17.

36. Pfeffer SR. LRRK2 and Rab GTPases. Biochemical Society Transactions. 2018 Nov 22;46(6):1707–12.

37. Hattula K, Furuhjelm J, Tikkanen J, Tanhuanpaa K, Laakkonen P, Peranen J. Characterization of the Rab8-specific membrane traffic route linked to protrusion formation. Journal of Cell Science. 2006 Nov 14;119(23):4866–77.

38. Sharma M, Giridharan SSP, Rahajeng J, Naslavsky N, Caplan S. MICAL-L1 links EHD1 to tubular recycling endosomes and regulates receptor recycling. Mol Biol Cell. 2009 Dec;20(24):5181–94.

39. Kobayashi H, Etoh K, Ohbayashi N, Fukuda M. Rab35 promotes the recruitment of Rab8, Rab13 and Rab36 to recycling endosomes through MICAL-L1 during neurite outgrowth. Biology Open. 2014 Sep 15;3(9):803–14.

40. Burtey A, Wagner M, Hodneland E, Skaftnesmo KO, Schoelermann J, Mondragon IR, et al. Intercellular transfer of transferrin receptor by a contact-, Rab8-dependent mechanism involving tunneling nanotubes. The FASEB Journal. 2015 Jul 28;29(11):4695–712.

41. Codazzi F, Pelizzoni I, Zacchetti D, Grohovaz F. Iron entry in neurons and astrocytes: a link with synaptic activity. Front Mol Neurosci [Internet]. 2015 [cited 2021 May 8];8. Available from: https://www.frontiersin.org/articles/10.3389/fnmol.2015.00018/full

42. Dringen R, Bishop GM, Koeppe M, Dang TN, Robinson SR. The pivotal role of astrocytes in the metabolism of iron in the brain. Neurochem Res. 2007 Nov;32(11):1884–90.

43. di Domenico A, Carola G, Calatayud C, Pons-Espinal M, Muñoz JP, Richaud-Patin Y, et al. Patient-Specific iPSC-Derived Astrocytes Contribute to Non-Cell-Autonomous Neurodegeneration in Parkinson's Disease. Stem Cell Reports. 2019 Feb 12;12(2):213–29.

44. Sonninen TM, Hämäläinen RH, Koskuvi M, Oksanen M, Shakirzyanova A, Wojciechowski S, et al. Metabolic alterations in Parkinson's disease astrocytes. Sci Rep. 2020 Sep 2;10(1):14474.

45. Pelizzoni I, Zacchetti D, Campanella A, Grohovaz F, Codazzi F. Iron uptake in quiescent and inflammation-activated astrocytes: A potentially neuroprotective control of iron burden. Biochim Biophys Acta. 2013 Aug;1832(8):1326–33.

46. You L, Yu PP, Dong T, Guo W, Chang S, Zheng B, et al. Astrocyte-derived hepcidin controls iron traffic at the blood-brain-barrier via regulating ferroportin 1 of microvascular endothelial cells. Cell Death Dis. 2022 Aug 1;13(8):1–12.

47. McCarthy RC, Kosman DJ. Glial Cell Ceruloplasmin and Hepcidin Differentially Regulate Iron Efflux from Brain Microvascular Endothelial Cells. PLOS ONE. 2014 Feb 12;9(2):e89003.

48. Sanyal A, DeAndrade MP, Novis HS, Lin S, Chang J, Lengacher N, et al. Lysosome and Inflammatory Defects in GBA1-Mutant Astrocytes Are Normalized by LRRK2 Inhibition. Mov Disord. 2020 May;35(5):760–73.

49. de Rus Jacquet A, Tancredi JL, Lemire AL, DeSantis MC, Li WP, O'Shea EK. The LRRK2 G2019S mutation alters astrocyte-to-neuron communication via extracellular vesicles and induces neuron atrophy in a human iPSC-derived model of Parkinson's disease. Bellen HJ, Zoghbi HY, editors. eLife. 2021 Sep 30;10:e73062.

50. Heo HY, Park JM, Kim CH, Han BS, Kim KS, Seol W. LRRK2 enhances oxidative stress-induced neurotoxicity via its kinase activity. Exp Cell Res. 2010 Feb 15;316(4):649–56.

51. Keeney MT, Rocha EM, Hoffman EK, Farmer K, Di Maio R, Weir J, et al. LRRK2 regulates production of reactive oxygen species in cell and animal models of Parkinson's disease. Science Translational Medicine. 2024 Oct 2;16(767):eadl3438.

52. Ilieva NM, Hoffman EK, Ghalib MA, Greenamyre JT, De Miranda BR. LRRK2 kinase inhibition protects against Parkinson's disease-associated environmental toxicants. Neurobiol Dis. 2024 Jun 15;196:106522.

53. Bennett DA, Buchman AS, Boyle PA, Barnes LL, Wilson RS, Schneider JA. Religious Orders Study and Rush Memory and Aging Project. J Alzheimers Dis. 2018;64(s1):S161–89.

54. Lagomarsino VN, Pearse RV, Liu L, Hsieh YC, Fernandez MA, Vinton EA, et al. Stem cell-derived neurons reflect features of protein networks, neuropathology, and cognitive outcome of their aged human donors. Neuron. 2021 Aug 26;S0896-6273(21)00578-X.

55. Beylina A, Langston RG, Rosen D, Reed X, Cookson MR. Generation of fourteen isogenic cell lines for Parkinson's disease-associated leucine-rich repeat kinase (LRRK2). Stem Cell Res. 2021 May;53:102354.

56. Mamais A, Sanyal A, Fajfer A, Zykoski CG, Guldin M, Riley-DiPaolo A, et al. The LRRK2 kinase substrates RAB8a and RAB10 contribute complementary but distinct disease-relevant phenotypes in human neurons. Stem Cell Reports. 2024 Feb 13;19(2):163–73.

57. Muratore CR, Zhou C, Liao M, Fernandez MA, Taylor WM, Lagomarsino VN, et al. Cell-type Dependent Alzheimer's Disease Phenotypes: Probing the Biology of Selective Neuronal Vulnerability. Stem Cell Reports. 2017 Dec 12;9(6):1868–84.

58. Paull D, Sevilla A, Zhou H, Hahn AK, Kim H, Napolitano C, et al. Automated, high-throughput derivation, characterization and differentiation of induced pluripotent stem cells. Nat Methods. 2015 Sep;12(9):885–92.

59. Canals I, Ginisty A, Quist E, Timmerman R, Fritze J, Miskinyte G, et al. Rapid and efficient induction of functional astrocytes from human pluripotent stem cells. Nature Methods. 2018 Sep;15(9):693–6.

60. Zhang Y, Pak C, Han Y, Ahlenius H, Zhang Z, Chanda S, et al. Rapid Single-Step Induction of Functional Neurons from Human Pluripotent Stem Cells. Neuron. 2013 Jun 5;78(5):785–98.

61. Sheta R, Teixeira M, Idi W, Pierre M, de Rus Jacquet A, Emond V, et al. Combining NGN2 programming and dopaminergic patterning for a rapid and efficient generation of hiPSC-derived midbrain neurons. Sci Rep. 2022 Oct 13;12(1):17176.

62. Sheta R, Teixeira M, Idi W, Oueslati A. Optimized protocol for the generation of functional human induced-pluripotent-stem-cell-derived dopaminergic neurons. STAR Protoc. 2023 Sep 15;4(3):102486.

63. Zhang DL, Ollivierre H, Rouault TA. Using Biotinylated Iron-Responsive Element to Analyze the Activity of Iron Regulatory Proteins. Int J Mol Sci. 2024 Apr 29;25(9):4852.

64. Madugula V, Lu L. A ternary complex comprising transportin1, Rab8 and the ciliary targeting signal directs proteins to ciliary membranes. J Cell Sci. 2016 Oct 15;129(20):3922–34.

65. Jones-Tabah J, He K, Karpilovsky N, Senkevich K, Deyab G, Pietrantonio I, et al. The Parkinson's disease risk gene cathepsin B promotes fibrillar alpha-synuclein clearance, lysosomal function and glucocerebrosidase activity in dopaminergic neurons. Mol Neurodegeneration. 2024 Nov 25;19(1):88.

66. Hirayama T, Miki A, Nagasawa H. Organelle-specific analysis of labile Fe(ii) during ferroptosis by using a cocktail of various colour organelle-targeted fluorescent probes†. Metallomics. 2019 Jan 23;11(1):111–7.

67. Tomita K, Fukumoto M, Itoh K, Kuwahara Y, Igarashi K, Nagasawa T, et al. MiR-7-5p is a key factor that controls radioresistance via intracellular Fe2+ content in clinically relevant radioresistant cells. Biochemical and Biophysical Research Communications. 2019 Oct 22;518(4):712–8.

68. Li X, Wang T, Huang X, Li Y, Sun T, Zang S, et al. Targeting ferroptosis alleviates methionine-choline deficient (MCD)-diet induced NASH by suppressing liver lipotoxicity. Liver International. 2020 Jun;40(6):1378–94.

69. Chen LL, Huang YJ, Cui J tao, Song N, Xie J. Iron dysregulation in Parkinson's disease: focused on the autophagy-lysosome pathway. ACS Chemical Neuroscience [Internet]. 2018 Dec 27 [cited 2019 Jan 2]; Available from: http://pubs.acs.org/doi/10.1021/acschemneuro.8b00390

70. Kurz T, Eaton JW, Brunk UT. The role of lysosomes in iron metabolism and recycling. The International Journal of Biochemistry & Cell Biology. 2011 Dec 1;43(12):1686–97.

71. Rizzollo F, More S, Vangheluwe P, Agostinis P. The lysosome as a master regulator of iron metabolism. Trends in Biochemical Sciences. 2021 Dec 1;46(12):960–75.

72. Eguchi T, Kuwahara T, Sakurai M, Komori T, Fujimoto T, Ito G, et al. LRRK2 and its substrate Rab GTPases are sequentially targeted onto stressed lysosomes and maintain their homeostasis. Proc Natl Acad Sci U S A. 2018 Sep 25;115(39):E9115–24.

73. Schapansky J, Nardozzi JD, Felizia F, LaVoie MJ. Membrane recruitment of endogenous LRRK2 precedes its potent regulation of autophagy. Hum Mol Genet. 2014 Aug 15;23(16):4201–14.

74. Liu Z, Bryant N, Kumaran R, Beilina A, Abeliovich A, Cookson MR, et al. LRRK2 phosphorylates membrane-bound Rabs and is activated by GTP-bound Rab7L1 to promote recruitment to the trans-Golgi network. Hum Mol Genet. 2018 15;27(2):385–95.

75. Niwa M, Hirayama T, Okuda K, Nagasawa H. A new class of high-contrast Fe(II) selective fluorescent probes based on spirocyclized scaffolds for visualization of intracellular labile iron delivered by transferrin. Org Biomol Chem. 2014 Aug 6;12(34):6590–7.

76. Cheng XT, Xie YX, Zhou B, Huang N, Farfel-Becker T, Sheng ZH. Characterization of LAMP1-labeled nondegradative lysosomal and endocytic compartments in neurons. J Cell Biol. 2018 Sep 3;217(9):3127–39.

77. Kluss JH, Beilina A, Williamson CD, Lewis PA, Cookson MR, Bonet-Ponce L. Lysosomal positioning regulates Rab10 phosphorylation at LRRK2+ lysosomes. Proceedings of the National Academy of Sciences. 2022 Oct 25;119(43):e2205492119.

78. Johnson DE, Ostrowski P, Jaumouillé V, Grinstein S. The position of lysosomes within the cell determines their luminal pH. Journal of Cell Biology. 2016 Mar 14;212(6):677–92.

79. Wallings R, Connor-Robson N, Wade-Martins R. LRRK2 interacts with the vacuolar-type H+-ATPase pump a1 subunit to regulate lysosomal function. Human Molecular Genetics. 2019 Aug 15;28(16):2696–710.

80. Rouault TA. The role of iron regulatory proteins in mammalian iron homeostasis and disease. Nat Chem Biol. 2006 Aug;2(8):406–14.

81. Pantopoulos K. Iron metabolism and the IRE/IRP regulatory system: an update. Ann N Y Acad Sci. 2004 Mar;1012:1–13.

82. Wallander ML, Leibold EA, Eisenstein RS. Molecular control of vertebrate iron homeostasis by iron regulatory proteins. Biochim Biophys Acta. 2006 Jul;1763(7):668–89.

83. Zhang DL, Ghosh MC, Rouault TA. The physiological functions of iron regulatory proteins in iron homeostasis - an update. Front Pharmacol. 2014;5:124.

84. Zhou ZD, Tan EK. Iron regulatory protein (IRP)-iron responsive element (IRE) signaling pathway in human neurodegenerative diseases. Mol Neurodegener [Internet]. 2017 Oct 23 [cited 2021 Jun 14];12. Available from: https://www.ncbi.nlm.nih.gov/pmc/articles/PMC5654065/

85. Thirstrup K, Dächsel JC, Oppermann FS, Williamson DS, Smith GP, Fog K, et al. Selective LRRK2 kinase inhibition reduces phosphorylation of endogenous Rab10 and Rab12 in human peripheral mononuclear blood cells. Sci Rep. 2017 Aug 31;7(1):10300.

86. Zhang P, Chen L, Zhao Q, Du X, Bi M, Li Y, et al. Ferroptosis was more initial in cell death caused by iron overload and its underlying mechanism in Parkinson's disease. Free Radical Biology and Medicine. 2020 May;152:227–34.

87. Angelova PR, Choi ML, Berezhnov AV, Horrocks MH, Hughes CD, De S, et al. Alpha synuclein aggregation drives ferroptosis: an interplay of iron, calcium and lipid peroxidation. Cell Death & Differentiation. 2020 Oct;27(10):2781–96.

88. Chen X, Comish PB, Tang D, Kang R. Characteristics and Biomarkers of Ferroptosis. Front Cell Dev Biol [Internet]. 2021 Jan 21 [cited 2021 May 14];9. Available from: https://www.ncbi.nlm.nih.gov/pmc/articles/PMC7859349/

89. Reichert CO, de Freitas FA, Sampaio-Silva J, Rokita-Rosa L, Barros P de L, Levy D, et al. Ferroptosis Mechanisms Involved in Neurodegenerative Diseases. Int J Mol Sci. 2020 Nov 20;21(22):8765.

90. Oun A, Soliman A, Trombetta-Lima M, Tzepapadaki A, Tsagkari D, Kortholt A, et al. LRRK2 protects immune cells against erastin-induced ferroptosis. Neurobiology of Disease. 2022 Dec 1;175:105917.

91. Z Z, S Z, X L, X W, C X, X W, et al. LRRK2 regulates ferroptosis through the system Xc-GSH-GPX4 pathway in the neuroinflammatory mechanism of Parkinson's disease. Journal of cellular physiology [Internet]. 2024 May [cited 2025 Mar 1];239(5). Available from: https://pubmed.ncbi.nlm.nih.gov/38477420/

92. Tian R, Abarientos A, Hong J, Hashemi SH, Yan R, Dräger N, et al. Genome-wide CRISPRi/a screens in human neurons link lysosomal failure to ferroptosis. Nat Neurosci [Internet]. 2021 May 24 [cited 2021 Jun 4]; Available from: http://www.nature.com/articles/s41593-021-00862-0

93. Forcina GC, Dixon SJ. GPX4 at the Crossroads of Lipid Homeostasis and Ferroptosis. Proteomics. 2019 Sep;19(18):e1800311.

94. Sato M, Kusumi R, Hamashima S, Kobayashi S, Sasaki S, Komiyama Y, et al. The ferroptosis inducer erastin irreversibly inhibits system xc− and synergizes with cisplatin to increase cisplatin's cytotoxicity in cancer cells. Sci Rep. 2018 Jan 17;8(1):968.

95. Xie Y, Hou W, Song X, Yu Y, Huang J, Sun X, et al. Ferroptosis: process and function. Cell Death Differ. 2016 Mar;23(3):369–79.

96. Zhao J, Xu B, Xiong Q, Feng Y, Du H. Erastin-induced ferroptosis causes physiological and pathological changes in healthy tissues of mice. Molecular Medicine Reports. 2021 Oct 1;24(4):1–8.

97. Sofic E, Riederer P, Heinsen H, Beckmann H, Reynolds GP, Hebenstreit G, et al. Increased iron (III) and total iron content in post mortem substantia nigra of parkinsonian brain. J Neural Transm. 1988;74(3):199–205.

98. Hirsch EC, Brandel JP, Galle P, Javoy-Agid F, Agid Y. Iron and aluminum increase in the substantia nigra of patients with Parkinson's disease: an X-ray microanalysis. J Neurochem. 1991 Feb;56(2):446–51.

99. Dexter DT, Wells FR, Agid F, Agid Y, Lees AJ, Jenner P, et al. Increased nigral iron content in postmortem parkinsonian brain. Lancet. 1987 Nov 21;2(8569):1219–20.

100. Bartzokis G, Cummings JL, Markham CH, Marmarelis PZ, Treciokas LJ, Tishler TA, et al. MRI evaluation of brain iron in earlier- and later-onset Parkinson's disease and normal subjects. Magn Reson Imaging. 1999 Feb;17(2):213–22.

101. Agola J, Jim P, Ward H, BasuRay S, Wandinger-Ness A. Rab GTPases as regulators of endocytosis, targets of disease and therapeutic opportunities. Clin Genet. 2011 Oct;80(4):305–18.

102. Greggio E, Jain S, Kingsbury A, Bandopadhyay R, Lewis P, Kaganovich A, et al. Kinase activity is required for the toxic effects of mutant LRRK2/dardarin. Neurobiol Dis. 2006 Aug;23(2):329–41.

103. Berndsen K, Lis P, Yeshaw WM, Wawro PS, Nirujogi RS, Wightman M, et al. PPM1H phosphatase counteracts LRRK2 signaling by selectively dephosphorylating Rab proteins. Harper W, Cole PA, Harper W, Newton AC, McPherson PS, editors. eLife. 2019 Oct 30;8:e50416.

104. West AB, Moore DJ, Choi C, Andrabi SA, Li X, Dikeman D, et al. Parkinson's disease-associated mutations in LRRK2 link enhanced GTP-binding and kinase activities to neuronal toxicity. Hum Mol Genet. 2007 Jan 15;16(2):223–32.

105. Dhekne HS, Yanatori I, Gomez RC, Tonelli F, Diez F, Schüle B, et al. A pathway for Parkinson's Disease LRRK2 kinase to block primary cilia and Sonic hedgehog signaling in the brain. Burd CG, Malhotra V, editors. eLife. 2018 Nov 6;7:e40202.

106. Vieweg S, Mulholland K, Bräuning B, Kachariya N, Lai YC, Toth R, et al. PINK1-dependent phosphorylation of Serine111 within the SF3 motif of Rab GTPases impairs effector interactions and LRRK2-mediated phosphorylation at Threonine72. Biochem J. 2020 May 15;477(9):1651–68.

107. Lai YC, Kondapalli C, Lehneck R, Procter JB, Dill BD, Woodroof HI, et al. Phosphoproteomic screening identifies Rab GTPases as novel downstream targets of PINK1. The EMBO Journal. 2015 Nov 12;34(22):2840–61.

108. Yin G, Lopes da Fonseca T, Eisbach SE, Anduaga AM, Breda C, Orcellet ML, et al. α-Synuclein interacts with the switch region of Rab8a in a Ser129 phosphorylation-dependent manner. Neurobiology of Disease. 2014 Oct;70:149–61.

109. Silva AMN, Rangel M. The (Bio)Chemistry of Non-Transferrin-Bound Iron. Molecules. 2022 Mar 9;27(6):1784.

110. Yambire KF, Rostosky C, Watanabe T, Pacheu-Grau D, Torres-Odio S, Sanchez-Guerrero A, et al. Impaired lysosomal acidification triggers iron deficiency and inflammation in vivo. Pfeffer SR, McPherson PS, editors. eLife. 2019 Dec 3;8:e51031.

111. Miles AL, Burr SP, Grice GL, Nathan JA. The vacuolar-ATPase complex and assembly factors, TMEM199 and CCDC115, control HIF1α prolyl hydroxylation by regulating cellular iron levels. Chacinska A, editor. eLife. 2017 Mar 15;6:e22693.

112. Manzoni C, Mamais A, Dihanich S, McGoldrick P, Devine MJ, Zerle J, et al. Pathogenic Parkinson's disease mutations across the functional domains of LRRK2 alter the autophagic/lysosomal response to starvation. Biochem Biophys Res Commun. 2013 Nov 29;441(4):862–6.

113. Eguchi T, Sakurai M, Wang Y, Saito C, Yoshii G, Wileman T, et al. The V-ATPase-ATG16L1 axis recruits LRRK2 to facilitate the lysosomal stress response. J Cell Biol. 2024 Mar 4;223(3):e202302067.

114. Feng Y, Wang X, Li P, Shi X, Prokosch V, Liu H. Exogenous hydrogen sulfide and NOX2 inhibition mitigate ferroptosis in pressure-induced retinal ganglion cell damage. Biochimica et Biophysica Acta (BBA) - Molecular Basis of Disease. 2025 Mar 1;1871(3):167705.

115. Wang Q, Liu J, Zhang Y, Li Z, Zhao Z, Jiang W, et al. Microglial CR3 promotes neuron ferroptosis via NOX2-mediated iron deposition in rotenone-induced experimental models of Parkinson's disease. Redox Biology. 2024 Nov 1;77:103369.

116. Nguyen HN, Byers B, Cord B, Shcheglovitov A, Byrne J, Gujar P, et al. LRRK2 mutant iPSC-derived DA neurons demonstrate increased susceptibility to oxidative stress. Cell Stem Cell. 2011 Mar 4;8(3):267–80.

117. Chen Y, Zhi L, Cui S, Wang H, Zeng C, Zhang H. The Human LRRK2-R1441G Mutation Drives Age-Dependent Oxidative Stress and Mitochondrial Dysfunction in Dopaminergic Neurons. bioRxiv. 2025 Jun 17;2025.06.16.660029.

118. Yue M, Hinkle KM, Davies P, Trushina E, Fiesel FC, Christenson TA, et al. Progressive dopaminergic alterations and mitochondrial abnormalities in LRRK2 G2019S knock-in mice. Neurobiol Dis. 2015 Jun;78:172–95.

119. Kurz T, Gustafsson B, Brunk UT. Intralysosomal iron chelation protects against oxidative stress-induced cellular damage. FEBS J. 2006 Jul;273(13):3106–17.

120. Boddu R, Hull TD, Bolisetty S, Hu X, Moehle MS, Daher JPL, et al. Leucine-rich repeat kinase 2 deficiency is protective in rhabdomyolysis-induced kidney injury. Hum Mol Genet. 2015 Jul 15;24(14):4078–93.

121. Dehestani M, Kessler W, Karmali N, Sun W, Volos P, Tsitkov S, et al. Single-cell transcriptomic changes in oligodendroglial lineage cells derived from Parkinson's disease patient-iPSCs with LRRK2-G2019S mutation [Internet]. bioRxiv; 2024 [cited 2025 Apr 7]. p. 2024.07.01.601392. Available from: https://www.biorxiv.org/content/10.1101/2024.07.01.601392v2

122. Zille M, Karuppagounder SS, Chen Y, Gough PJ, Bertin J, Finger J, et al. Neuronal Death After Hemorrhagic Stroke In Vitro and In Vivo Shares Features of Ferroptosis and Necroptosis. Stroke. 2017 Apr;48(4):1033–43.

123. Goldman A, Nguyen M, Lanoix J, Fahmy A, Xu YZ, Schurr E, et al. LRRK2G2019S acts as a dominant interfering mutant in the context of iron overload [Internet]. bioRxiv; 2025 [cited 2026 Jan 21]. p. 2025.08.25.672135. Available from: https://www.biorxiv.org/content/10.1101/2025.08.25.672135v1

124. Ke Y, Ho K, Du J, Zhu L, Xu Y, Wang Q, et al. Role of soluble ceruloplasmin in iron uptake by midbrain and hippocampus neurons. Journal of Cellular Biochemistry. 2006;98(4):912–9.

125. Booth HDE, Hirst WD, Wade-Martins R. The Role of Astrocyte Dysfunction in Parkinson's Disease Pathogenesis. Trends Neurosci. 2017 Jun;40(6):358–70.

126. Dzamko N, Gysbers AM, Bandopadhyay R, Bolliger MF, Uchino A, Zhao Y, et al. LRRK2 levels and phosphorylation in Parkinson's disease brain and cases with restricted Lewy bodies. Movement Disorders. 2017;32(3):423–32.

127. Khan SS, Jaimon E, Lin YE, Nikoloff J, Tonelli F, Alessi DR, et al. Loss of primary cilia and dopaminergic neuroprotection in pathogenic LRRK2-driven and idiopathic Parkinson's disease. Proceedings of the National Academy of Sciences. 2024 Aug 6;121(32):e2402206121.

128. Hogarth P. Neurodegeneration with Brain Iron Accumulation: Diagnosis and Management. J Mov Disord. 2015 Jan;8(1):1–13.

129. Romano N, Baiardi G, Pinto VM, Quintino S, Gianesin B, Sasso R, et al. Long-Term Neuroradiological and Clinical Evaluation of NBIA Patients Treated with a Deferiprone Based Iron-Chelation Therapy. J Clin Med. 2022 Aug 3;11(15):4524.

130. Iankova V, Karin I, Klopstock T, Schneider SA. Emerging Disease-Modifying Therapies in Neurodegeneration With Brain Iron Accumulation (NBIA) Disorders. Front Neurol [Internet]. 2021 Apr 15 [cited 2025 Apr 7];12. Available from: https://www.frontiersin.org/journals/neurology/articles/10.3389/fneur.2021.629414/full

131. Schneider SA, Bhatia KP. Excess iron harms the brain: the syndromes of neurodegeneration with brain iron accumulation (NBIA). J Neural Transm. 2013 Apr 1;120(4):695–703.

132. Devos D, Rascol O, Meissner WG, Foubert-Samier A, Lewis S, Tranchant C, et al. Therapeutic modalities of deferiprone in Parkinson's disease: SKY and EMBARK studies. Journal of Parkinson's Disease. 2025 Feb 1;15(1):72–86.